Calibration of a 35-GHz Airborne Cloud Radar: Lessons Learned and Intercomparisons with 94-GHz Cloud Radars

Florian Ewald[1], **Silke Groß**[1], **Martin Hagen**[1], **Lutz Hirsch**[2], **Julien Delanoë**[3], **and Matthias Bauer-Pfundstein**[4]

[1]Deutsches Zentrum für Luft und Raumfahrt, Institut für Physik der Atmosphäre, Oberpfaffenhofen, Germany
[2]Max Planck Institute for Meteorology, Hamburg, Germany
[3]LATMOS/UVSQ/IPSL/CNRS, Guyancourt, France
[4]Metek GmbH, Elmshorn, Germany

Correspondence: Florian Ewald (florian.ewald@dlr.de)

Abstract. This study gives a summary of lessons learned during the absolute calibration of the airborne, high-power Ka-band cloud radar *HAMP MIRA* on board the German research aircraft HALO. The first part covers the internal calibration of the instrument where individual instrument components are characterized in the laboratory. In the second part, the internal calibration is validated with external reference sources like the ocean surface backscatter and different air- and spaceborne cloud radar instruments.

A key component of this work was the characterization of the spectral response and the transfer function of the receiver. In a wide dynamic range of $70\,\mathrm{dB}$, the receiver response turned out to be very linear (residual $0.05\,\mathrm{dB}$). Using different attenuator settings, it covers a wide input range from $-105\,\mathrm{dBm}$ to $-5\,\mathrm{dBm}$. This characterization gave valuable new insights about the receiver sensitivity and additional attenuations which led to a major improvement of the absolute calibration. The comparison of the measured and the previously estimated total receiver noise power ($-95.3\,\mathrm{dBm}$ vs. $-98.2\,\mathrm{dBm}$) revealed an underestimation of $2.9\,\mathrm{dB}$. This underestimation could be traced back to a larger receiver noise bandwidth of $7.5\,\mathrm{MHz}$ (instead of $5\,\mathrm{MHz}$) and a slightly higher noise figure ($1.1\,\mathrm{dB}$). Measurements confirmed the previously assumed antenna gain ($50.0\,\mathrm{dBi}$) with no obvious asymmetries or increased sidelobes. The calibration used for previous campaigns, however, did not accounted for a $1.5\,\mathrm{dB}$ two-way attenuation by additional waveguides in the airplane installation. Laboratory measurements also revealed a $2\,\mathrm{dB}$ higher two-way attenuation by the belly pod caused by small deviations during manufacturing. In total, effective reflectivities measured during previous campaigns had to be corrected by $+7.6\,\mathrm{dB}$.

To validate this internal calibration, the well defined ocean surface backscatter was used as a calibration reference. With the new absolute calibration, the ocean surface backscatter measured by HAMP MIRA agrees very well ($< 1\,\mathrm{dB}$) with modeled values and values measured by the GPM satellite. As a further cross-check, flight experiments over Europe and the tropical North-Atlantic were conducted. To that end, a joint flight of HALO and the French Falcon 20 aircraft, which was equipped with the RASTA cloud radar at $94\,\mathrm{GHz}$ and an underflight of the spaceborne CloudSat at $94\,\mathrm{GHz}$ were performed. The intercomparison revealed lower reflectivities ($-1.4\,\mathrm{dB}$) for RASTA but slightly higher reflectivities ($+1.0\,\mathrm{dB}$) for CloudSat. With effective reflectivities between RASTA and CloudSat and the good agreement with GPM, the accuracy of the absolute calibration is estimated to be around $1\,\mathrm{dB}$.

1 Introduction

In recent years, the deployment of cloud profiling microwave radars on the ground, on aircraft as well as on satellites, like CloudSat (Stephens et al., 2002) or the upcoming Earth-CARE satellite mission (Illingworth et al., 2014), greatly advanced our scientific knowledge of cloud microphysics. Nevertheless, large discrepancies in retrieved cloud microphysics (Zhao et al., 2012; Stubenrauch et al., 2013) contribute to uncertainties in the understanding of the role of clouds for the climate system (Boucher et al., 2013). An important aspect for enabling accurate microphysical retrievals based on cloud radar data is the proper calibration of the systems.

However, the absolute calibration of an airborne millimeter-wave cloud radar can be a challenging task. Its initial calibration demands a detailed knowledge of cloud radar technology and the availability of suitable measurement devices. During cloud radar operation, system parameters of transmitter and receiver system can drift due to changing ambient temperature, pressure and aging system components. The validation of the absolute calibration with external sources is furthermore complicated for downward-looking installations on an aircraft. The missing ability of most airborne and many ground-based radars to point their line of sight to an external reference source makes it difficult or even completely impossible to calibrate the overall system with an external reference in a laboratory.

Typically, an budget approach is used for the absolute calibration of airborne cloud radar instruments. First, the instrument components like transmitter, receiver, waveguides, antenna and radome are characterized individually in the laboratory. During in-flight measurements, variable component parameters are then monitored and corrected for drifts using the laboratory characterization. Subsequently, all gains and losses are combined into an overall instrument calibration.

In order to meet the required absolute accuracy and to follow good scientific practice, an external in-flight calibration becomes indispensable to check the internal calibration for systematic errors. For weather radars, the well-defined reflectivity of calibration spheres on tethered balloons or erected trihedral corner reflectors has been a reliable external reference for years (Atlas, 2002). In more recent years, this technique is being extended to scanning, ground-based millimeter-wave radars (Vega et al., 2012; Chandrasekar et al., 2015). For the airborne perspective on the other hand, the direct fly-over and the subsequent removal of additional background clutter is difficult to reproduce (Li et al., 2005b).

Driven by this challenge, many studies have been conducted to characterize the characteristic reflectivity of the ocean surface using microwave scatterometer-radiometer systems in the X- and Ka-band (Valenzuela, 1978; Masuko et al., 1986). As one of the first, Caylor (1994) introduced the ocean surface backscatter technique to cross-check the internal calibration of the NASA ER-2 Doppler radar (EDOP; Heymsfield et al., 1996). In an important next step, Li et al. (2005a) combined this technique with analytical models of the ocean surface backscatter. In their work, they used circle and roll maneuvers to sample the ocean surface backscatter for different incidence angles with the Cloud Radar System (CRS; Li et al., 2004), a 94-GHz (W band) cloud radar on board the NASA ER-2 high-altitude aircraft. In this context, they proposed to point the instrument $10°$ off-nadir; an angle for which multiple studies found a very constant ocean surface backscatter (Durden et al., 1994; Li et al., 2005b; Tanelli et al., 2006). For this incidence angle, these studies confirmed the ocean surface to be relatively insensitive to changes in wind speed and wind direction.

Subsequent studies followed suit, applying the same technique to other airborne cloud radar instruments: the Japanese W-band Super Polarimetric Ice Crystal Detection and Explication Radar (SPIDER; Horie et al., 2000) on board the NICT Gulfstream II by Horie et al. (2004), the Ku/Ka-band Airborne Second Generation Precipitation Radar (APR-2; Sadowy et al., 2003) on board the NASA P-3 aircraft by Tanelli et al. (2006) and the W-band cloud radar (RASTA; Protat et al., 2004) on board the SAFIRE Falcon-20 by Bouniol et al. (2008).

Encouraged by these airborne studies, this in-flight calibration technique has also been proposed and successfully applied to the spaceborne CloudSat instrument (Stephens et al., 2002; Tanelli et al., 2008). Based on this success, Horie and Takahashi (2010) proposed the same technique with a whole $10°$ sweep across track for the next spaceborne cloud radar, the $94\,\mathrm{GHz}$ Doppler Cloud Profiling Radar (CPR) on board EarthCARE (Illingworth et al., 2014).

With CloudSat as a long term cloud radar in space, direct comparisons of radar reflectivity from ground- and airborne instruments became possible (Bouniol et al., 2008; Protat et al., 2009). While first studies still assessed the stability of the spaceborne instrument, subsequent studies turned this around by using CloudSat as a Global Radar Calibrator for ground-based or airborne radars Protat et al. (2010).

This work will focus on the internal and external calibration of the MIRA cloud radar (Mech et al., 2014) on board the German *High Altitude and Long Range Research Aircraft* (HALO), adopting the ocean surface backscattering technique described by Li et al. (2005b). In the first part, the pre-flight laboratory characterization of each system component will be described. This includes antenna gain, component attenuation and receiver sensitivity. In a budget approach, these system parameters are then used in combination with in-flight monitored transmission and receiver noise power levels to form the internal calibration. The second part will then compare the internal calibration with external reference sources in-flight. As external reference sources, measurements of the ocean surface as well as inter-comparisons with other air- and spaceborne cloud radar instruments will be used.

This paper is organized as follows: After some considerations about required radar accuracies shown in Sec. 1.1, Section 2 introduces the cloud radar instrument and its specifications on board the HALO research aircraft. Section 3 recalls the radar equation and introduces the concept of using the ocean surface backscatter for radar calibration. The characterization and calibration of the single system components, from waveguides, antenna to belly pod is described in Section 3.1. Subsequently, the overall calibration of the radar receiver is explained in Section 3.2. Here, a central innovation of this work is the determination of the receiver sensitivity (Section 3.3 and 3.4). In the second part of the paper, the budget calibration is validated by using predicted and measured ocean surface backscatter (Section 4.3). In addition,
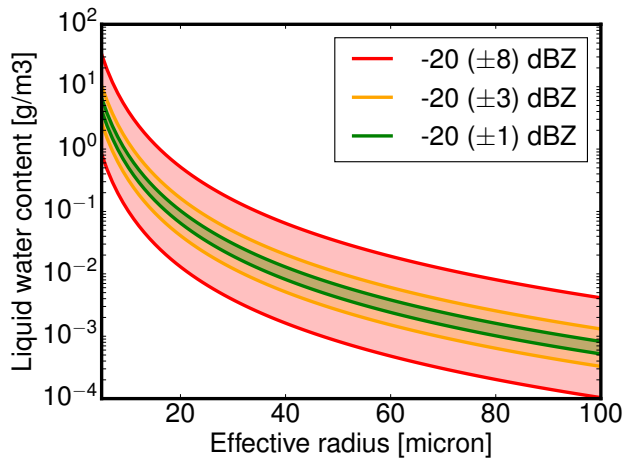
Figure 1. Microphysical retrieval uncertainty due to different absolute calibration uncertainties ($\pm1, \pm3, 8\pm$) for mono-disperse cloud water droplets according to Mie calculations.

the calibration and system performance for joint flight legs is compared to the W-band cloud radars like the airborne cloud radar RASTA (Section 5.2) and the spaceborne cloud radar CloudSat (Section 5.3).

1.1 Accuracy considerations

In order to provide scientifically sound interpretations of cloud radar measurements, a well-calibrated instrument with known sensitivity is indispensable. Many spaceborne (Delanoë and Hogan, 2008; Deng et al., 2010) or ground-based (Donovan et al., 2000) techniques to retrieve cloud microphysics using millimeter-wave radar measurements require a well calibrated instrument. In the case of the CloudSat instrument, the calibration uncertainty was specified to be ±2 dB or better (Stephens et al., 2002). This requirement for absolute calibration imposed by retrievals of cloud microphysics is further explained in Fig. 1. Under the simplest assumption of small, mono-disperse cloud water droplets, the iso-lines in Fig. 1 represent all combinations of cloud droplet effective radius and liquid water content with a radar reflectivity of -20 dBz. An increasing retrieval ambiguity, caused by an assumed instrument calibration uncertainty, is illustrated by the shaded areas with ±1 dB (green), ±3 dB (yellow) and ±8 dB (red). To constrain the retrieval space considerably within synergistic radar-lidar retrievals like Cloudnet (Illingworth et al., 2007) or Varcloud (Delanoë and Hogan, 2008), the absolute calibration uncertainty has to be significantly smaller than the natural variability of clouds. Since a reflectivity bias of 8 dB would bias the droplet size by a factor of 2 and the water content by even a magnitude, the absolute calibration uncertainty should be at least 3 dB or lower. For a systematic 1 dB calibration offset, Protat et al. (2016) still found ice water content biases of $+19\%$ and -16% in their radar-only retrieval. Since HAMP MIRA data is used in re-

trievals of cloud microphysics, the target accuracy will be set to 1 dB.

An accurate absolute calibration is further motivated by recent studies (Protat et al., 2009; Hennemuth et al., 2008; Maahn and Kollias, 2012; Ewald et al., 2015; Lonitz et al., 2015; Myagkov et al., 2016; Acquistapace et al., 2017), which used the radar reflectivity provided by almost identical ground-based versions of the same instrument. The installation of the MIRA instrument on many ground-based cloud profiling sites within ACTRIS (Aerosols, Clouds and Trace gases Research InfraStructure Network; http://www.actris.net) and in the framework of Cloudnet is a further incentive for an external calibration study.

The need for an external calibration is furthermore encouraged by several studies which already found evidences of an offset in radar reflectivity when comparing different cloud radar instruments. In a direct comparison with the W-Band (94 GHz) ARM Cloud Radar (WACR), Handwerker and Miller (2008) found around 3 dB smaller reflectivities for the Karlsruhe Institute of Technology MIRA, contradicting the reflectivity reducing effect of a higher gaseous attenuation and stronger Mie scattering at 94 GHz. Protat et al. (2009) could reproduce this discrepancy in a comparison with CloudSat, where they found a clear systematic shift of the mean vertical profile by 2 dB between Cloudsat and the Lindenberg MIRA (CloudSat showing higher values than the Lindenberg radar).

2 The 35-GHz cloud radar on HALO

The cloud radar on HALO is a pulsed Ka-band, polarimetric Doppler millimeter-wavelength radar which is based on prototypes developed and described by Bormotov et al. (2000) and Vavriv et al. (2004). The current system was manufactured and provided by *Metek* (Meteorologische Messtechnik GmbH, Elmshorn, Germany). The system design and its data processing, including an updated moment estimation and a target classification by Bauer-Pfundstein and Görsdorf (2007) was described in detail by Görsdorf et al. (2015). The millimeter radar is part of the HALO Microwave Package (HAMP) which will be subsequently abbreviated as *HAMP MIRA*. Its standard installation in the belly pod section of HALO with its fixed nadir-pointing 1 m diameter Cassegrain antenna is described in detail by Mech et al. (2014). Its transmitter is a high-power magnetron operating at 35.5 GHz with a peak power P_t of 27 kW, with a pulse repetition frequency f_p between 5–10 kHz and a pulse width τ_p between 100–400 ns. The large antenna and the high peak power can yield an exceptionally good sensitivity of -47 dBZ for the ground-based operation (5 km distance, 1 s averaging and a range resolution of 30 m). In the current airborne configuration, the sensitivity is reduce to -39.8 dBZ by various circumstances which will be addressed in this paper. The broadening of the Doppler spectrum due to the beam width can reduce this sen-

Table 1. Technical specifications of the HAMP cloud radar as characterized in this work. Boldface indicates the operational configuration used in this work.

Parameter	Variable	Value
Wavelength	λ	8.45 mm
Pulse Power	P_t	27 kW
Pulse Repetition	f_p	**5 − 10** kHz
Pulse Width	τ_p	100, **200**, 400 ns
Recieve Window	τ_r	100, **200**, 400 ns
RF Noise Bandwidth	B_n	**7.5**, 5 MHz
RF Front-End Noise Figure	NF	9.9 dB
RF Front-End Sensitivity	P_n	−95.3 dBm
Sensitivity[*] (ground)	$Z_{\min}$	−47.5 dBZ
Sensitivity[*] (airborne)	$Z_{\min}$	−39.8 dBZ
Antenna Gain	G_a	50.0 dB
Beamwidth (3 dB)	ϕ	0.56°
Atten. (Finite Bandwith)	L_{fb}	1.2 dB
Atten. (Tx Path)	L_{rx}	0.75 dB
Atten. (Rx Path)	L_{tx}	0.75 dB
Atten. (Belly pod)	L_{bp}	1.5 dB

[*] at 5 km, 1 s avg., 30 m res.

sitivity further by $9\,\mathrm{dB}$ as discussed in Mech et al. (2014). Table 1 lists the technical specifications as characterized in this work. Boldface indicates the operational configuration.

Most of the parameters in Table 1 play a role for the absolute calibration of the cloud radar instrument. For this reason, this section will briefly recapitulate the conversion from receiver signal power to the commonly used equivalent radar reflectivity factor Z_e. When the radar reflectivity η of a target is known, e.g. in modeling studies, its equivalent radar reflectivity factor is given by

$$Z_e = \frac{\eta \lambda^4}{|K|^2 \pi^5} \tag{1}$$

where $|K|^2 = 0.93$ is the dielectric factor for water and λ the radar wavelength. For brevity, the equivalent radar reflectivity factor Z_e is referred to as "effective reflectivity" in this paper. Following the derivation of the meteorological form of the radar equation by Doviak and Zrnić (1993), the effective reflectivity $Z_e\,(\mathrm{mm}^6\mathrm{m}^{-3})$ can be calculated from the received signal power $P_r\,(\mathrm{W})$ by

$$Z_e = R_c P_r r^2 L_{\mathrm{atm}}^2 \tag{2}$$

where r is the range between antenna and target, L_{atm} is the one-way path integrated attenuation, and R_c is a constant which describes all relevant system parameters. Assuming a circularly symmetric Gaussian antenna pattern, this radar constant R_c contains the pulse wavelength $\lambda\,(\mathrm{m})$, pulse width $\tau_p\,(\mathrm{s})$ and peak transmit power P_t in milliwatts, the peak antenna gain G_a and the antenna half-power beamwidth ϕ. It additionally accounts for all attenuations L_{sys} occurring in system components, e.g. in transmitter (L_{tx}) and receiver

(L_{rx}) waveguides, due to the belly pod radome L_{bp}^2 and due to the finite receiver bandwidth (L_{fb}):

$$R_c = \frac{1024 \ln 2 \lambda^2 10^{18} L_{\mathrm{sys}}}{P_t G_a^2 c \tau_p \pi^3 \phi^2 |K|^2} \tag{3}$$

Usually, antenna parameters (G_a, ϕ) and system losses ($L_{\mathrm{sys}} = L_{\mathrm{tx}} L_{\mathrm{bp}}^2 L_{\mathrm{rx}}$) have to be determined only once for each system modification. In contrast, transmitter and receiver parameters have to be monitored continuously. In addition, a thorough characterization of the receiver sensitivity is essential for the absolute accuracy of the instrument.

3 Internal/Budget calibration

This section will discuss the internal calibration of the radar instrument and its characterization in the laboratory. The following section will then compare this budget approach in-flight with an external reference source.

The monitoring of the system specific parameters and the subsequent estimation of effective reflectivity is described in detail by Görsdorf et al. (2015). The internal calibration (budget calibration) strategy for the HAMP MIRA is therefore only briefly summarized here. In case of a deviation, previously assumed and used parameters will be given and referred as *initial calibration* for traceability of past radar measurements.

3.1 Antenna, radome and waveguides

- *Antenna*: The gain $G_a = 50.0\,\mathrm{dBi}$ and the beam pattern ($-3\,\mathrm{dB}$ beamwidth $\phi = 0.56°$) was determined by the manufacturer following the procedure described by Myagkov et al. (2015). Hereby the $1\,\mathrm{m}$ diameter Cassegrain antenna was installed on a pedestal to scan its pattern on a tower $400\,\mathrm{m}$ away. The antenna pattern showed no obvious asymmetries or increased sidelobes (sidelobe level: $-22\,\mathrm{dB}$). Its characterization revealed no significant differences in comparison with the initially estimated parameters ($G_a = 49.75\,\mathrm{dBi}$, $\phi = 0.6°$).

- *Radome*: The thickness of the epoxy quartz radome in the belly pod was designed with a thickness of $4.53\,\mathrm{mm}$ to limit the one-way attenuation to around $0.5\,\mathrm{dB}$. Deviations during manufacturing increased the thickness to $4.84\,\mathrm{mm}$, with a one-way attenuation of around $1.5\,\mathrm{dB}$. Laboratory measurements confirmed this $2.0\,\mathrm{dB}$ ($2 \times 1.0\,\mathrm{dB}$) higher two-way attenuation compared to the initially used value for the radome attenuation. A detailed analysis of this deviation can be found in Appendix B.

- *Waveguides*: The initially used calibration did not accounted for the losses caused by the longer waveguides in the airplane installation. Actually, transmitter and receiver waveguides each have a length of $1.15\,\mathrm{m}$. With a

specified attenuation of $0.65\,\mathrm{dB/m}$, the two-way attenuation by waveguides is thus $1.5\,\mathrm{dB}$.

3.2   Transmitted and received signal power

- *Transmitter peak power P_t*: Due to strong variations in ambient temperatures in the cabin, in-flight thermistor measurements proved to be unreliable. For this reason, thermally controlled measurements of P_t were conducted on ground which were correlated with measured magnetron currents I_m. The relationship between both parameters then allowed to derive P_t from in-flight measurements of I_m. A detailed analysis of this relationship can be found in Appendix A.

- *Finite receiver bandwidth loss L_{fb}*: The loss caused by a finite receiver bandwidth was discussed in detail by Doviak and Zrnić (1979). For a Gaussian receiver response, the finite receiver bandwidth loss L_{fb} can be estimated using

$$L_{\mathrm{fb}} = -10\log_{10}\left(\coth(2b) - \frac{1}{2b}\right) \quad \text{with:} \quad b = \frac{\pi B_6 \tau_p}{4\sqrt{\ln 2}}$$
(4)

Here, B_6 is the $6\,\mathrm{dB}$ filter bandwidth of the receiver and τ_p is the duration of the pulse. During the initial calibration, no correction of the finite receiver bandwidth loss was applied.

- *Signal-to-Noise (SNR)*: For eached sampled range, MIRA's digital receiver converts phase shifts of consecutive pulse trains (e.g. $N_P = 256$ pulses) into power spectra of Doppler velocities v_i by a real-time fast Fourier transform (FFT). First, spectral densities $s_j(v_i)$ of multiple power spectra are averaged (e.g. $N_S = 20$ spectra) to enhance the signal-to-noise ratio. Subsequently, the averaged spectral densities $\overline{s_j}(v_i)$ in individual velocity bins are summed to yield a total received signal S in each gate:

$$\overline{s}(v_i) = \frac{1}{N_S} \sum_{j=1}^{j=N_S} s_j(v_i)$$
(5)

$$S = \sum_{i=1}^{i=N_P} \overline{s}(v_i)\,\Delta v_i$$
(6)

The receiver chain omits a separate absolute power meter circuit. At the end of each pulse cycle, the receiver is switched to internal reference gates by a pin diode in front of the first amplifier. These two last gates are called the receiver noise gate and the calibration gate. To obtain the received backscattered signal S_r in atmospheric gates, one has to substract the signal received in the noise gate S_{ng} from the total received signal S since it contains both signal and noise:

$$S_r = S - S_{\mathrm{ng}}$$
(7)

In that way, a signal-to-noise ratio is then calculated by dividing the received backscattered signal S_r in each atmospheric gate by the signal S_{ng} measured in the noise gate:

$$\mathrm{SNR}^\dagger = \frac{S_r}{S_{\mathrm{ng}}}$$
(8)

The relative power of the calibration gate to the receiver noise gate is furthermore used to monitor the receiver sensitivity (for details see Sec. 3.3). The main advantage of this method is the simultaneous monitoring of the relative receiver sensitivity using the same circuitry that is used for atmospheric measurements. Furthermore, the determination of the receiver noise in a separate noise gate can prevent biases in SNR, when the noise floor in atmospheric gates is obscured by aircraft motion or strong signals, both leading to a broadened Doppler spectrum.

Following (Riddle et al., 2012), the minimum $\mathrm{SNR}_{\mathrm{min}}$ can be calculated in terms of N_P and N_S, if the backscattered signal power is contained in a single Doppler velocity bin:

$$\mathrm{SNR}_{\mathrm{min}} = \frac{Q}{N_P\sqrt{N_S}}.$$
(9)

Here, $Q = 7$ is a threshold factor between the received signal and the standard deviation of the noise signal. In the absence of any turbulence- or motion-induced Doppler shift, the operational configuration yields a $\mathrm{SNR}_{\mathrm{min}}$ of $-22.1\,\mathrm{dB}$. As discussed in Mech et al. (2014), this minimum SNR can be larger by $9\,\mathrm{dB}$ due to a motion-induced broadening of the Doppler spectrum in the airborne configuration.

- *Received signal power P_r*: The SNR response of the receiver to an input power P_r is described by a receiver transfer function $\mathrm{SNR} = \mathcal{T}(P_r)$. When $\mathcal{T}$ is known, an unknown received signal power P_r can be derived from a measured SNR by the inversion $\mathcal{T}^{-1}$:

$$P_r = \mathcal{T}^{-1}(\mathrm{SNR})$$
(10)

- *Receiver sensitivity P_n*: For a linear receiver, $\mathcal{T}^{-1}$ can be approximated by a signal-independent receiver sensitivity P_n, which translates a measured SNR to an absolute signal power P_r in dBm:

$$P_r \approx P_n\,\mathrm{SNR}$$
(11)

More specifically, P_n can be interpreted as an overall receiver noise power and is thus equal to the power of the smallest measurable white signal. It includes the inherent thermal noise within the receiver response, the overall noise figure of the receiver and mixer circuitry and all losses occurring between ADC and receiver input.
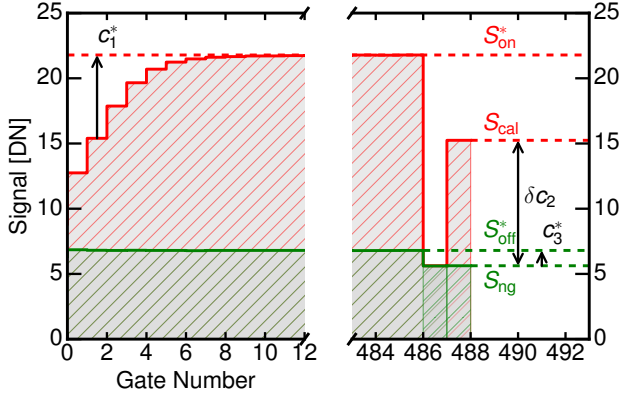
Figure 2. Total received signal S in digital numbers as a function of gate number with external noise source switched on (S_{on}^*, red) and switched off (S_{off}^*, green). The two last gates monitor the signals S_{ng} and S_{cal}, which correspond to the receiver noise and the internal calibration source. The factors c_1^*, c_2 and c_3^* correct the estimated noise power $P_n^\dagger$ to reflect the actual receiver sensitivity P_n. Signal levels obtained only during the calibration with the external noise source are marked with an asterisk.

3.3 Estimated Receiver Sensitivity

Prior to this work, no rigorous determination of the receiver transfer function $\mathcal{T}$ was performed. During the initial calibration, the receiver sensitivity P_n was instead estimated using the inherent thermal noise and its own noise characteristic.

Generated by thermal electrons, the inherent thermal noise P_{kTB} received by a matched receiver can be derived using Boltzmann's constant k_B, temperature T_0 and the noise bandwidth B_n of the receiver. Additional noise power is introduced by the electronic circuitry itself, which is considered by the receiver noise factor F_n. The noise factor F_n expressed in decibels (dB) is called noise figure NF. Combined, P_{kTB} and F_n yield the total inherent noise power $P_n^\dagger$:

$$P_n^\dagger = P_{kTB} F_n = k_B T_0 B_n F_n \quad [W] \tag{12}$$

Using a calibrated external noise source with known excess noise ratio (ENR), F_n was determined in the laboratory. In-flight, F_n is monitored using the calibration and the noise gate.

In the following, measurements obtained with the calibrated external noise source in the laboratory are marked with an asterisk. Signal levels measured in-flight as well as during the calibration are marked without an asterisk. Figure 2 shows the external noise source measurements, where the received signal S is plotted as a function of the gate number. While connected to the receiver input, the external noise source is switched on and off with signals $S_{\mathrm{on}}^*(r)$ (red) and $S_{\mathrm{off}}^*(r)$ (green) measured in atmospheric gates. Corresponding to this, S_{cal}^* and S_{ng}^* are the signals measured in the two last gates, namely the calibration and the receiver noise gates.

The in-flight signals in these two reference gates are denoted by S_{cal} and S_{ng}.

Using the so called *Y-factor method* (Agilent, 2004), the averaged noise floor ratio Y in atmospheric gates between the external noise source being switched on and off and the ENR of the external noise source are used to determine the noise factor F_n created by the receiver components:

$$F_n = \frac{\mathrm{ENR}}{Y-1} \quad \text{with} \quad Y = \frac{\langle S_{\mathrm{on}}^*(r)\rangle}{\langle S_{\mathrm{off}}^*(r)\rangle} \tag{13}$$

Here, the averaging $\langle S_{\mathrm{on}}^*(r)\rangle$ of atmospheric gates is done for gate numbers larger than 10 to exclude the attenuation caused by the transmit/receive switch immediately after the magnetron pulse. During the initial calibration with the external noise source, a noise figure NF = 8.8 dB was determined.

Summarizing the above considerations, an overall receiver sensitivity $P_n^\dagger$ is estimated using an assumed receiver noise bandwidth of 5 MHz, a receiver temperature of 290 K and a noise figure of NF = 8.8 dB. According to Eq. 12, the estimated receiver sensitivity $P_n^\dagger$ used in the initial calibration is

$$P_n^\dagger = -98.2 \quad [\mathrm{dBm}] \tag{14}$$

The measurements with the external noise source are furthermore exploited to correct for various effects, which cause deviations between the inherent noise power $P_n^\dagger$ in the noise gate and the actual receiver sensitivity P_n:

$$P_n = c_1^* c_2 P_n^\dagger \tag{15}$$

Here,

- c_1^* accounts for the attenuation in atmospheric gates, which is caused by the transmit/receive switch immediately after the magnetron pulse:

$$c_1^*(r) = \frac{\langle S_{\mathrm{on}}^*(r) - S_{\mathrm{off}}^*(r)\rangle}{S_{\mathrm{on}}^*(r) - S_{\mathrm{off}}^*(r)} \tag{16}$$

As evident in Fig. 2, c_1^* is only significant in the first 8 range gates (= 240 m) and rapidly converges to 0 dB in the remaining atmospheric and reference gates.

- Secondly, the correction factor c_2 is used to monitor and correct in-flight drifts of the receiver sensitivity. To this end, the ratio $S_{\mathrm{cal}}^*/S_{\mathrm{ng}}^*$ measured during calibration between calibration and noise gate is compared to the ratio $S_{\mathrm{cal}}/S_{\mathrm{ng}}$ during flight:

$$c_2 = \frac{S_{\mathrm{cal}}^*/S_{\mathrm{ng}}^*}{S_{\mathrm{cal}}/S_{\mathrm{ng}}} \tag{17}$$

In the course of one flight of several hours, c_2 varies only slightly by ±0.5 dB. Continuous observation of c_2 should be performed to keep track on the receiver sensitivity.

– A further factor accounts for the fact that the noise level measured in the noise gate is lower than the total system noise with matched load because the low-noise amplifier is not matched during the noise gate measurement. The signal-to-noise $SNR^\dagger$ determined with the noise gate level therefore overestimates the actual signal-to-noise SNR in atmospheric gates:

$$SNR = c_3^* SNR^\dagger \tag{18}$$

In Fig. 2, this offset is called c_3^*. Its value is determined by comparing the signal S_{ng}^* in the noise gate with the signal S_{off}^* in atmospheric gates, while the external noise source is switched off:

$$c_3^* = \frac{S_{ng}^*}{S_{off}^*} \tag{19}$$

This offset between noise gate and total system noise remains very stable with $c_3^* = -0.83\,dB$. Since c_3^* exists only in earlier MIRA-35 systems (without MicroBlaze processor, e.g. KIT, UFS, HALO and Lindenberg), most MIRA-35 operators do not have to address this issue.

3.4 Measured Receiver Sensitivity

A key component of this work was to replace the estimated receiver sensitivity $P_n^\dagger$ with an actual measured value P_n. While $P_n^\dagger$ was calculated using an assumed receiver noise bandwidth and the receiver noise factor, P_n is now measured directly using a calibrated signal generator with adjustable power and frequency output. By varying the power at the receiver input, P_n is found as the noise equivalent signal when $SNR = 0\,dB$. In addition, the receiver response and its bandwidth is determined by varying the frequency of the signal generator. Both measurements are then used to evaluate and check F_n according to Eq.12. This is done for two different matched filter lengths ($\tau_r = 100\,ns$, $\tau_r = 200\,ns$) to characterize the dependence of B_n and F_n on τ_r.

To this end, an analog continuous wave signal generator *E8257D* from *Agilent Technologies* was used to determine the receiver's spectral response and its power transfer function $\mathcal{T}$. The signal generator was connected to the antenna port of the radar receiver and tuned to $35.5\,GHz$, the central frequency of the local oscillator. For the characterization, the radar receiver was set into standard airborne operation mode. In this mode, 256 samples are averaged coherently into power spectra by FFT. Subsequently, 20 power spectra are then averaged to obtain a smoothed power spectrum for each second.

3.4.1 Receiver Bandwidth

To determine the spectral response, the frequency sweep mode of the signal generator with a fixed signal amplitude was used within a region of $35500 \pm 20\,MHz$. For the shorter match filter length ($\tau_r = 100\,ns$) and the left and for

the longer matched filter length ($\tau_r = 200\,ns$) on the right, Fig. 3 shows measured signal-to-noise ratios as a function of the frequency offset from the center frequency at $35.5\,GHz$. The spectral response of the receiver for both matched filters (black lines) approaches a Gaussian fit (crosses). To estimate the finite receiver bandwidth loss L_{fb} using Eq. 4, the $6\,dB$ filter bandwidth (two-sided arrow) is determined directly from the receiver response with $B_6 = 9.8\,MHz$ for $\tau_r = 200\,ns$ and $B_6 = 17.2\,MHz$ for $\tau_r = 100\,ns$, respectively. In the following, the equivalent noise bandwidth (ENBW) concept is used to determine the receiver noise bandwidth B_n which is needed to calculate P_n In short, the ENBW is the bandwidth of a rectangular filter with the same received power as the actual receiver. Illustrated by the green and blue hatched rectangles in Fig. 3, the measured ENBW is $B_{n,200} = 7.5\,MHz$ for the longer matched filter length and $B_{n,100} = 13.5\,MHz$ for the shorter matched filter length. In contrast, the red-hatched rectangles show the estimated $5\,MHz$ (resp. $10\,MHz$) receiver noise bandwidth using $1/\tau_r$. The discrepancy between the measured and the estimated noise bandwidth could be traced back to an additional window function which was applied unintentionally to IQ data within the digital signal processor. This issue led to a bit more thermal noise power P_{kTB}. For the operationally used matched filter ($\tau_r = 200\,ns$), the offset between estimated and actual thermal noise power ($-106.9\,dBm$ vs. $-105.2\,dBm$) led to an $1.8\,dB$ underestimation of Z_e. Future measurements will not include this bias since this issue was found and fixed.

3.4.2 Receiver Transfer Function

Next, the amplitude ramp mode of the signal generator was used to determine the transfer function $P_r = \mathcal{T}(SNR)$ of the receiver. The receiver transfer function references absolute signal powers at the antenna port with corresponding SNR values measured by the receiver. Moreover, the linearity and cut-offs of the receiver can be assessed on the basis of the transfer function. For this measurement, the frequency of the signal generator was set to $35.5\,GHz$, while the output power of the generator was increased steadily from $-110\,dBm$ to $10\,dBm$. This was done in steps of $1\,dBm$ while averaging over 10 power spectra. In order to test the linearity and the saturation behavior of the receiver for strong signals, this measurements were repeated with an internal attenuator set to $15\,dB$ and $30\,dB$. For $\tau_r = 200\,ns$, Fig. 4a shows the measured receiver transfer functions for the three attenuator settings of $0\,dB$ (black), $15\,dB$ (green) and $30\,dB$ (red). For measurements with activated attenuator, SNR values have been corrected by $+15\,dB$ (respectively $+30\,dB$) to compare the transfer functions to the one with $0\,dB$ attenuation. The overlap of the different transfer functions between input powers of $-70\,dBm$ and $-30\,dBm$ in Fig. 4a confirms the specified attenuator values of $15\,dB$ and $30\,dB$. Furthermore, no further saturation by additional receiver components (e.g.
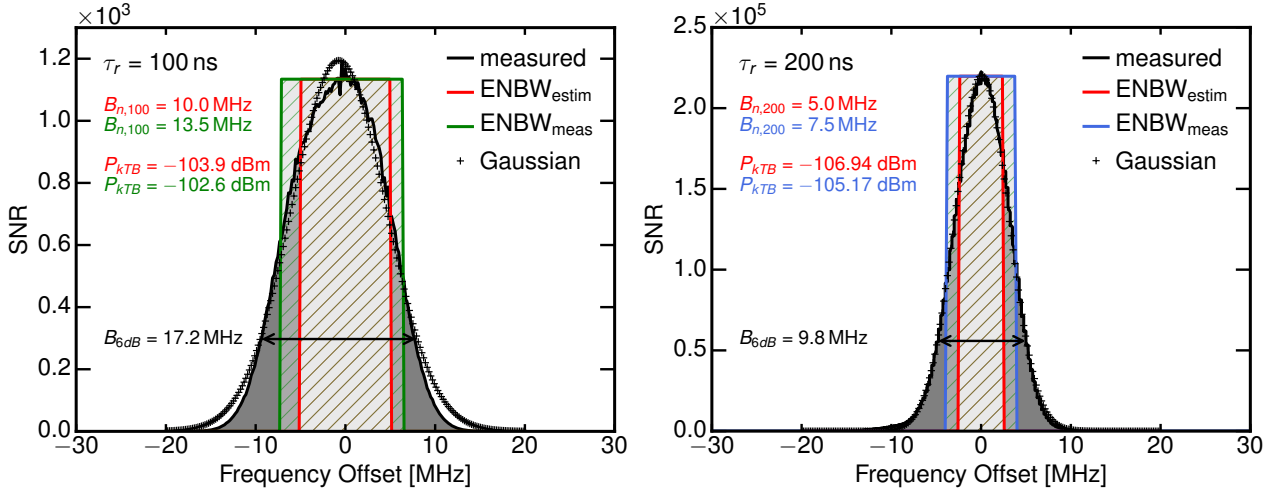
Figure 3. Measured radar receiver response (gray) as a function of the frequency offset from the center frequency at $35.5\,\text{GHz}$ for two different matched filter lengths. While the green and blue hatched rectangles show the actual equivalent noise bandwidths, the red-hatched rectangles show the estimated noise bandwidth that was used in the initial calibration.
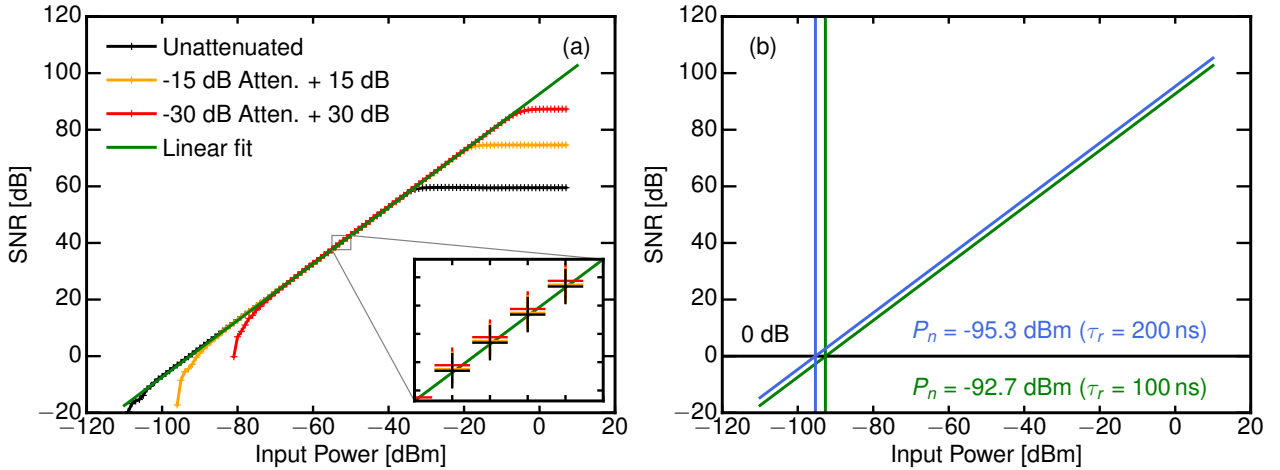
Figure 4. (a) Measured receiver transfer functions for the three attenuator settings of $0\,\text{dB}$ (black), $15\,\text{dB}$ (green) and $30\,\text{dB}$ (red). **(b)** Linear regression receiver transfer function to determine the receiver sensitivity P_n.

mixers or filters) can be detected up to an input power of $-5\,\text{dBm}$. This allows to shift the dynamic range by using the attenuator to measure higher input powers (which would otherwise be saturated) without losing the absolute calibration. This feature is essential for the evaluation of very strong signals like the ground return.

Subsequently, a linear regression to the results without attenuator was performed between input powers of $-70\,\text{dBm}$ and $-40\,\text{dBm}$, which is shown in Fig. 4b.

$$\text{SNR} = \mathcal{T}(P_r) \approx mP_r - P_n \quad [dB] \qquad (20)$$

With a slope m of $1.0009\,(\pm0.0006)$ and a residual of $0.054\,\text{dB}$, the receiver behaved very linearly for this input power region. Similar values were obtained for an attenuation of $+15\,\text{dB}$ with a slope of $0.9980\,(\pm0.0005)$ and a resid-

ual of $0.024\,\text{dB}$ and a slope of $0.9884\,(\pm0.0013)$ and a residual of $0.1\,\text{dB}$ for an attenuation of $+30\,\text{dB}$.

3.4.3 Receiver Sensitivity

Finally, the linear regression to the receiver transfer function can be used to derive the receiver sensitivity P_n. Its x-intercept ($\text{SNR} = 0$) directly yields the receiver sensitivity P_n for the two matched filter lengths:

$$P_n = -92.7\,\text{dBm} \qquad (\tau_r = 100\,\text{ns}) \qquad (21)$$
$$P_n = -95.3\,\text{dBm} \qquad (\tau_r = 200\,\text{ns}) \qquad (22)$$

As discussed before, the setting with the shorter matched filter length collects more thermal noise due to the larger receiver bandwidth. In a final step, this top-down approach to

obtain P_n for different τ_r can be used to determine F_n and check for its dependence on τ_r. By solving Eq. 12 for F_n and inserting the measured bandwidths B_{100} and B_{200} we obtain:

$$P_n / P_{kTB} = F_n \tag{23}$$

$$-92.7\,\text{dBm} + 102.6\,\text{dBm} = 9.9\,\text{dB} \qquad (\tau_r = 100\,\text{ns}) \tag{24}$$

$$-95.3\,\text{dBm} + 105.2\,\text{dBm} = 9.9\,\text{dB} \qquad (\tau_r = 200\,\text{ns}) \tag{25}$$

Remarkably, F_n shows no dependence on τ_r but turns out to be larger than prev384ously estimated by $1.1\,\text{dB}$. This previous underestimation of F_n led to an $1.1\,\text{dB}$ underestimation of Z_e.

Now, all system parameters are known to estimate the radar sensitivity at a particular range. Following Doviak and Zrnić (1993), the minimum detectable effective reflectivity $Z_{\min}(r)$ at a particular range can be calculated using Eq. 2 in decibel:

$$Z_{\min}(r) = \text{MDS} + 20\log_{10} r + \log_{10} R_c \tag{26}$$

Here, P_r is the minimum detectable signal MDS in dBm which is given by $P_n\,\text{SNR}_{\min}$ using Eq. 11:

$$\text{MDS} = P_n\,\text{SNR}_{\min} \tag{27}$$

In the operational configuration ($Q = 7$, $N_P = 256$, $N_S = 20$), the MDS is $-117.4\,\text{dBm}$, since $\text{SNR}_{\min} = -22.1\,\text{dB}$ and $P_n = -95.3\,\text{dBm}$. The parameters listed in Table 1 yield a range-independent radar constant of $R_c = 3.9\,\text{dB}$. Using the MDS and R_c in Eq. 26, the minimum detectable effective reflectivity in $5\,\text{km}$ is $Z_{\min}(5\,\text{km}) = -39.8\,\text{dBZ}$.

3.5 Overall calibration budget

Comparing the measured $P_n = -95.3\,\text{dBm}$ to the estimated $P_n^\dagger = -98.2\,\text{dBm}$ for $\tau_r = 200\,\text{ns}$, the combination of bandwidth bias ($1.8\,\text{dB}$) and larger noise figure ($1.1\,\text{dB}$) caused an $2.9\,\text{dB}$ underestimation of Z_e. Combined with the non-application of the $2.0\,\text{dB}$ higher two-way attenuation by the radome, the $1.5\,\text{dB}$ higher two-way attenuation by the waveguides and including the finite receiver bandwidth loss $L_{\text{fb}} = 1.2\,\text{dB}$, effective reflectivities Z_e derived with the initial calibration have to be corrected by $+7.6\,\text{dB}$. Table 2 summarizes and breaks down all offsets found in this work.

4 External calibration using the ocean surface backscatter

The following section will now test the absolute calibration using an external reference target. As already mentioned in the introduction, the ocean surface has been used as a calibration standard for air- and spaceborne radar instruments. In their studies, Barrick et al. (1974) and Valenzuela (1978) reviewed and harmonized theories to describe the interaction of electro-magnetic waves with the ocean surface. They showed

Table 2. Breakdown of the offset between original and new calibration for each system parameter. Values for $L_{\text{rx+tx}}$ and L_{fb} were already known but not applied in past measurement campaigns. The total offset has to be applied to R_c and Z_e.

Parameter	Original	This study	Offset
$L_{\text{rx+tx}}$	-	1.5 dB	+1.5 dB
L_{fb}	-	1.2 dB	+1.2 dB
L_{bp}^2	1.0 dB	3.0 dB	+2.0 dB
G_{a}	49.75 dBi	50.0 dBi	-0.5 dB
ϕ_{a}	0.6°	0.56°	+0.6 dB
P_n	-98.2 dBm	-95.3 dBm	
NF	8.8 dB	9.9 dB	+1.1 dB
B_n	5 MHz	7.5 MHz	+1.8 dB
Total			+7.6 dB

that the normalized radar cross-section σ_0 of the ocean surface at small incidence angles ($\Theta < 15°$) can be described by quasi-specular scattering theory. At larger incidence angles ($\Theta > 15°$), Bragg scattering at capillary waves becomes dominant, which complicates and enhances the backscattering of microwaves by ocean waves.

4.1 Modeling the normalized radar cross-section of the ocean surface

At the scales of millimeter waves and for small incidence angles θ, the ocean surface slope distribution is assumed to be Gaussian and isotropic, where the surface mean square slope $s(v)$ is a sole function of the wind speed v and independent from wind direction. Backscattered by ocean surface *facets*, which are aligned normal to the incidence waves (Plant, 2002), the normalized radar cross-section σ_0 can be described as a function of ocean surface wind speed v and beam incidence angle θ (Valenzuela, 1978; Brown, 1990; Li et al., 2005b):

$$\sigma_0(v, \theta, \lambda) = \frac{|\Gamma_e(0, \lambda)|^2}{s(v)^2 \cos^4(\theta)} \exp\left[-\frac{\tan^2(\theta)}{s(v)^2}\right] \tag{28}$$

For the ocean surface facets at normal incidence, the reflection of microwaves is described by an effective Fresnel reflection coefficient $\Gamma_e(0, \lambda) = C_e \frac{[n(\lambda)-1]}{[n(\lambda)+1]}$. In this study, the complex refractive index $n(\lambda = 8.8\,\text{mm}) = 5.565 + 2.870i$ for seawater at $25\,°\text{C}$ is used following the model by Klein and Swift (1977). Like with other models (Ray, 1972; Meissner and Wentz, 2004), the impact of salinity on σ_0 is negligible, while the influence of the ocean surface temperature on σ_0 stays below $\Delta\sigma_0 = 0.5\,\text{dB}$ between $5\,°\text{C}$ and $30\,°\text{C}$. Since specular reflection is only valid in the absence of surface roughness, various studies (Wu, 1990; Jackson, 1992; Freilich and Vanhoff, 2003; Li et al., 2005a) included an *correction factor* C_e to describe the reflection of microwaves

on wind-roughened water facets. While C_e has been well characterized for the Ku-band (Apel, 1994; Freilich and Vanhoff, 2003) and W-band (Horie et al., 2004; Li et al., 2005a), experimental results valid for the Ka-band are scarce (Nouguier et al., 2016). Tanelli et al. (2006) used simultaneous measurements of σ_0 in the Ku- and Ka-band, to determine $|\Gamma_e(0, \lambda = 8.8\mathrm{mm})|^2 = 0.455$ for the Ka-band, which corresponds to an correction factor C_e of 0.90. However, there is an ongoing discussion about an influence of radar wavelength or wind speed on C_e (Jackson, 1992; Tanelli et al., 2008). Chen et al. (2000) explains this disagreement with the different surface mean square slope statistics used in these studies, which do not include ocean surface roughness at the millimeter scale. To include this uncertainty in this study, the correction factor C_e has been varied between 0.85 and 0.95, while the simple model (CM) for non-slick ocean surfaces by Cox and Munk (1954) was used for $s(v)$. In their model, the surface mean square slope $s(v)$ scales linearly with wind speed v, describing a smooth ocean surface including gravity and capillary waves:

$$s(v)^2 = 0.003 + 5.08 \times 10^{-3} v \qquad (29)$$

4.2 Measuring the normalized radar cross-section of the ocean surface

The ocean surface backscatter is also measured by the Global Precipitation Measurement (GPM; Hou et al., 2013) platform which carries a Ku-/Ka-band dual-frequency precipitation radar (DPR). For this study, σ_0^* from GPM is used as an independent source to support the calculated σ_0 from the model. Operating at $35.5\,\mathrm{GHz}$, the KaPR scans the surface backscatter with its 0.7° beamwidth phased array antenna resulting in a $120\,\mathrm{km}$ swath of $5\,\mathrm{km} \times 5\,\mathrm{km}$ footprints. The measured ocean surface backscatter by GPM is operationally used to retrieve surface wind conditions and path-integrated attenuation of the radar beam. In the following, the σ_0^* corrected for gaseous attenuation from GPM was used which corresponds to the co-localized matched swath of the KaPR.

During the second *Next Generation Remote Sensing for Validation Studies* (NARVAL2) in June-August 2016, HAMP MIRA was deployed on HALO. The campaign was focused on the remote sensing of organized convection over the tropical North Atlantic Ocean in the vicinity of Barbados. Another campaign objective was the integration and validation of the new remote sensing instruments on board the HALO aircraft. For the HAMP MIRA cloud radar, multiple roll- and circle-maneuvers at different incidence angles were included in research flights to implement the well established calibration technique to measure the normalized radar cross-section of the ocean surface at different incidence angles.

During NARVAL2, HAMP MIRA was installed in the belly pod section of HALO and aligned in a fixed nadir-pointing configuration with respect to the airframe. The incidence angle is therefore controlled by pitch-and-roll maneuvers of the aircraft. The aircraft position and attitude are pro-

vided at a $10\,\mathrm{Hz}$ rate by the *BAsic HALO Measurement And Sensor System* (BAHAMAS; Krautstrunk and Giez, 2012). Pitch, roll and yaw angles are provided with an accuracy of 0.05°, while the absolute uncertainty can be up to 0.1°. Additional incidence angle uncertainty is caused by uncertainties in the alignment of the radar antenna. Following the approach of Haimov and Rodi (2013), the apparent Doppler velocity of the ground was used to determine the antenna beam-pointing vector. With this technique, the offsets from nadir with respect to the airframe was determined with 0.5° to the left in roll direction and 0.05° forward in pitch direction.

During calibration patterns, HALO flew at $9.7\,\mathrm{km}$ altitude with a ground speed of $180\,\mathrm{ms}^{-1}$ to $200\,\mathrm{ms}^{-1}$. The pulse repetition frequency was kept at $6\,\mathrm{kHz}$ with a pulse length of $\tau_p = 200\,\mathrm{ns}$. For the purpose of calibration, the data processing and averaging was set to $1\,\mathrm{Hz}$, being the standard campaign setting with Doppler spectra averaged from 20 FFTs which each contain 256 pulses. As a consequence of this configuration, the ocean surface backscatter at nadir was sampled in gates measuring approx $100\,\mathrm{m}$ in the horizontal and $30\,\mathrm{m}$ in the vertical. With this gate geometry, a uniform beam-filling of the ocean surface is ensured for incidence angles below 20°.

In the current configuration, the point target spread function of the matched receiver is under-sampled since the sampling is matched to the gate length. Thus, the maximum of the ocean backscatter can become underestimated when the surface is located between two gates. At nadir incidence, negative bias of σ_0 of up to $3 - 4\,\mathrm{dB}$ were observed in earlier measurement campaigns, when the gate spacing equals or is larger than the pulse length (Caylor et al., 1997). For this reason, the received power from the range gates below and above were added to the received power of the strongest surface echo. By adding the power from only three gates, Caylor et al. (1997) could reduce the uncertainty in σ_0 to $1\,\mathrm{dB}$ and exclude the contribution by antenna side-lobes from larger ranges.

Furthermore, the backscattered signal was corrected for gaseous attenuation by oxygen and water vapor considered in the loss factor L_{atm}. While the two-way attenuation by oxygen and water vapor is normally almost negligible in the Ka-band, it has to be considered in subtropical regions with high humidity and temperature near the surface. To this end, the gaseous absorption model for millimeter waves by Rosenkranz (1998) was used. Sounding profiles of pressure, temperature and humidity were provided by *Vaisala RD-94* dropsondes, which were launched from HALO during the calibration maneuvers.

Following Li et al. (2005a), the measured normalized cross-section σ_0^* of the ocean surface can be calculated from measured signal-to-noise-ratios:

$$\sigma_0^* = \frac{c \pi^5 \tau_p R_c r^2 L_{\mathrm{atm}}^2}{2 \lambda^4 10^{18}} P_n \mathrm{SNR} \qquad (30)$$
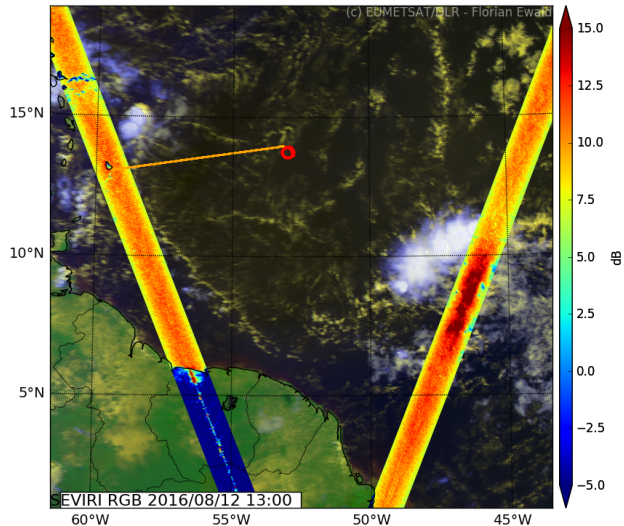
Figure 5. Flight track in orange with a true color image taken during that time by the geostationary SEVIRI instrument. The red circle marks the circular flight section shown in Fig. 6. The superimposed color-map shows the Ka-band σ_0^* measured by GPM in the vicinity of the operating area.

Here, the receiver power P_r was replaced with $P_n \text{SNR}$ (Eq. 10) to include the overall receiver sensitivity P_n in the formulation of σ_0^*. Like in Eq. 2, R_c is the radar constant (with $|K|^2 = 1$) which includes the transmitter power P_t, transmitting and receiving waveguide loss L_{tx} and L_{rx}, attenuation by the belly pod L_{bp} and the antenna gain G_a. Together with P_n, the combination of these system parameters are being checked in the following section, when the measured σ_0^* is compared to the modeled σ_0. For the following analysis, σ_0^* was obtained with Eq. 30 using 1 Hz-averaged SNR from HAMP MIRA.

4.3   Comparison of measurements and model

The HAMP MIRA calibration maneuver during NARVAL2 was included into research flight RF03 on 12 August 2016. The flight took place 700 km east from Barbados in a region of a relatively pronounced dry intrusion with light winds and very little cloudiness. Fig. 5 shows the flight track in orange with a true color image taken during that time by the geostationary SEVIRI instrument. The superimposed color-map shows σ_0^* from GPM in the vicinity of the operating area for that day. Here, the satellite nadir is located in the center of each track, with inclination angles $\theta > 0$ left and right towards the edges of the swath. Apparently, σ_0^* seems spatially quite homogeneous, where the ocean surface is only covered by small marine cumulus clouds. The first way-point was chosen to be collocated with a meteorological buoy ($14.559°N, 53.073°W$, NDBC 41040) to obtain the accurate wind-speed and direction at the level of the ocean surface as well as wave heights measured by the buoy. At 12:50
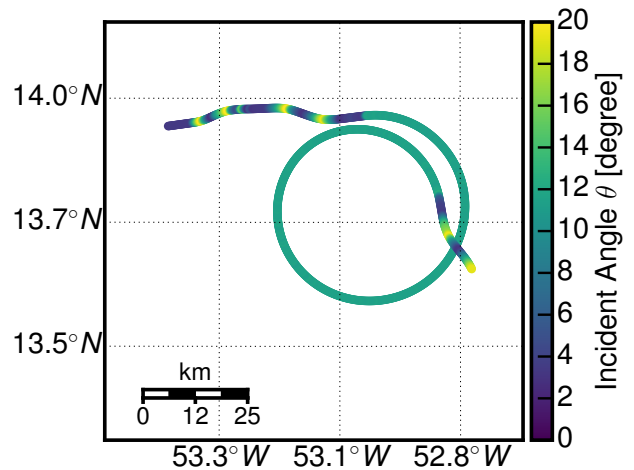
Figure 6. Overview of the flight path during the calibration maneuver with the beam incidence angle θ shown by the color-map.

UTC, the buoy measured a wind-speed of $5.7\,\text{m/s}$ from $98°$ with a mean wave height of $1\,\text{m}$ and mean wave direction of $69°$. A detailed overview of the flight path during the calibration maneuver is shown in Fig. 6, where the beam incidence angle θ is shown by the color-map. At 12:40 UTC, the aircraft executed a set of $\pm 20°$ roll maneuvers to sample σ_0^* in the cross-wind direction. At 12:44 UTC, the aircraft entered a right-hand turn with a constant roll angle of $10°$, the incidence angle for which σ_0^* becomes insensitive to surface wind conditions and models. After a full turn at 12:58 UTC, another set of $\pm 20°$ roll maneuvers were executed to sample σ_0^* in the along-wind direction. The dropsonde was launched around 13:06 UTC at $12.98°N$ and $52.78°W$. A two-way attenuation by water vapor and oxygen absorption L_{atm}^2 of $0.78\,\text{dB}$ was calculated using the dropsonde sounding. With an approximate distance of $700\,\text{km}$, the GPM measurement closest to the calibration area was made at 10:46:29 UTC at $13.67°N$ and $59.53°W$. To obtain a representative σ_0^* measurement from GPM, the swath data was averaged along-track for 10 seconds.

The measurement of σ_0^* during the across-wind roll maneuver is shown in Fig. 7a. The blue circles mark the corresponding GPM measurements. For the HAMP MIRA data, σ_0^* was calculated using the old, estimated calibration (red dots) and the new, measured calibration (green dots). In order to assess the agreement of σ_0^* with σ_0, the CM model for σ_0 (Eq. 28) was first calculated using the measured wind speed from the buoy. This values are shown by the black line in Fig. 7a. The shaded region around this line illustrates the uncertainty in σ_0 due to the uncertainty in C_e ($0.85 \ldots 0.95$). Both, modeled as well as measured σ_0 show the exponential falloff with θ corresponding to the smaller mean square slope of the ocean surface with increasing θ. In a second step, the CM model was fitted to σ_0^* from the old (red line) and new (green line) calibration to obtain the wind speed v. Here, a
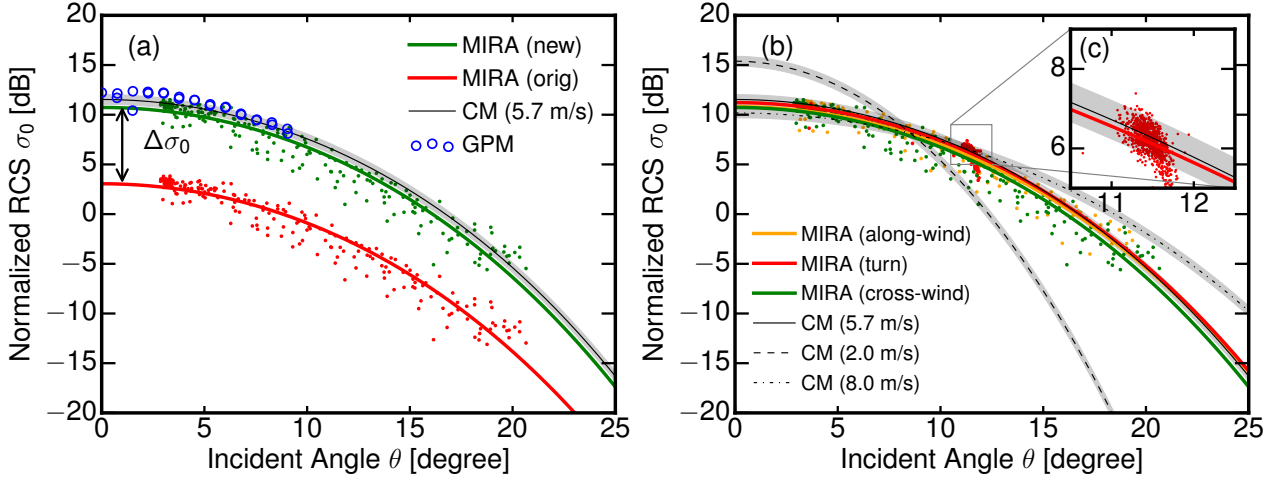
Figure 7. Normalized radar cross-section (RCS) σ_0^* of the ocean surface as a function of the radar beam incident angle θ. **(a)** Falloff of σ_0^* with θ measured with HAMP MIRA (red/green dots) and GPM (blue circles). The HAMP MIRA data is calculated and subsequently fitted using the old, estimated calibration (red line) and the new, measured calibration (green line). The modeled value (CM: Cox-Munk) and uncertainty of σ_0 for the actual measured wind speed from the buoy is shown by the black line and the shaded region. **(b)** Comparison of measured σ_0^* during the along-wind (orange) and across-wind (green) roll maneuver and during the turn (red). **(c)** A closer on the scatter of σ_0 during the turn maneuver with a standard deviation of $0.8\,\mathrm{dB}$.

potential calibration offset $\Delta\sigma_0$ was considered as a second fitting parameter:

$$\sigma_0^* = \sigma_0(v, \theta, \lambda) + \Delta\sigma_0 \qquad (31)$$

The following analysis is valid for the turn maneuver; differences between across-wind roll, turn and along-wind roll maneuver are discussed in the Fig. 7b and the following paragraph. For old and new calibration, the fitted wind speed of $5.71\,\mathrm{m/s}$ agrees very well with the actual measured wind speed of $5.7\,\mathrm{m/s}$. While σ_0^* for the old calibration shows a strong underestimation of σ_0 by $\Delta\sigma_0 = -7.8\,\mathrm{dB}$, the fit for the new calibration only marginally underestimates σ_0 with $\Delta\sigma_0 = -0.2\,\mathrm{dB}$, well within the uncertainty of σ_0. Thus, the initial calibration yields $7.6\,\mathrm{dB}$ smaller values for σ_0^* when compared to the new calibration that is in good agreement with the modeled values. This observed difference also matches precisely with the $7.6\,\mathrm{dB}$ difference determined during the absolute calibration in Sec. 3. Furthermore, the accuracy of the new absolute calibration is supported by the GPM measurements in the vicinity. With an increasing offset $\Delta\sigma_0$ from $-0.1\,\mathrm{dB}$ to $-1\,\mathrm{dB}$ towards smaller incidence angles, GPM measured only slightly larger values within its $9°$ co-localized matched swath compared to the new absolute calibration. Here, the small, increasing offset $\Delta\sigma_0$ with decreasing θ suggests a slightly lower wind speed at the GPM footprint, with more ocean surface facets pointing into the backscatter direction. The much better agreement of the new absolute calibration with GPM is a further demonstration of its validity.

Extending this discussion, the dependence of σ_0^* on wind direction is tested in the following study. To this end, Fig. 7b

shows σ_0^* measured during the across-wind (green) and along-wind (red) roll maneuver as well as during the turn. Like in Fig. 7a, the CM model for the actual measured wind speed of $5.7\,\mathrm{m/s}$ is fitted to the $1\,\mathrm{Hz}$-averaged σ_0^* measured during the three flight patterns. While the across-wind results are slightly below the values of σ_0 predicted by the wind speed of the buoy by $\Delta\sigma_0 = -0.5\,\mathrm{dB}$, the along-wind results underestimate σ_0 by $\Delta\sigma_0 = -0.8\,\mathrm{dB}$. In comparison, the fit to the measurements in the turn showed the smallest offset $\Delta\sigma_0 = -0.2,\mathrm{dB}$. The inset in Fig. 7c gives a closer on the scatter of σ_0 during the turn maneuver with a standard deviation of $0.8\,\mathrm{dB}$. Here, the slightly higher values were measured in the downwind section of the turn; an observation that is in line with measurements by Tanelli et al. (2006). In addition, this scatter is further caused by the under-sampled point target spread function of the ocean surface with a remaining uncertainty of $1\,\mathrm{dB}$. Due to these two effects, the measured σ_0^* will be associated with an uncertainty of $1\,\mathrm{dB}$. To put a possible directional dependence in perspective to the effect of different wind speeds, modeled σ_0 are plotted with their uncertainty for wind speeds of $2\,\mathrm{m/s}$ (dashed line), $8\,\mathrm{m/s}$ (dashed-dotted line) and the actual $5.7\,\mathrm{m/s}$ (solid line). In summary, measured σ_0^* for the new calibration agree with modeled as well as independently measured values within their uncertainty estimates.

5 Inter-comparison with RASTA and CloudSat

The following section will validate the preceding external calibration. To that end, we conducted common flight legs with W-Band cloud radars, like the airborne *RASTA* and the

spaceborne *CloudSat*. First, possible differences between effective reflectivities at 35 GHz and 94 GHz are explored on the basis of a numerical study.

5.1 Model study of Z_e at 35 and 94 GHz

In contrast to water cloud droplets, ice crystals have various shapes and sizes. With increasing maximum diameter D_{max}, ice crystals become more complex and their effective density decreases (Heymsfield et al., 2010). For this study, we use the "composite" mass-size relationship from Heymsfield et al. (2010) (Eq. 10, in their paper) to describe the connection between the maximum ice crystal diameter D_{max} and its equivalent melted diameter D_{eq}. This relationship combines data sets of six in situ measurement campaigns in a variety of ice cloud types. We assumed horizontally aligned oblate spheroids with an aspect ratio of 0.6, composed of a mixture of air and ice which follows the given mass-size relationship. As a function of the equivalent melted diameter D_{eq}, the ice fraction of this mixture is shown as green line in Figure 8. Furthermore, a realistic and well tested particle size distribution (PSD) is used. Since PSDs are known to be highly variable (Intrieri et al., 1993), we choose the normalized PSD approach by Delanoë et al. (2005) which is based on an extensive database of airborne in situ measurements. Figure 8 shows this PSD as a function of D_{eq} for different effective ice crystal radii r_{eff}. Following Delanoë et al. (2014), the effective radius is derived using Foot (1988) which increases proportional to the ratio of mass to projected area. The mass-size relationship and PSD are also a key component of the synergistic radar-lidar retrieval DARDAR (Delanoë et al., 2014) which is designated for the EarthCARE mission.

In the following, 'Rayleigh scattering only' will be compared to Mie scattering and T-Matrix scattering theory. Mie theory is applied assuming homogeneous ice-air spheres, while the T-Matrix calculations are done for the spheroids of same mass and area as the ice-air spheres.

The model results for a single ice crystal are shown in Fig. 9a. Here, the effective reflectivities at 35 GHz (green) and 94 GHz (red) are shown as a function of equivalent melted diameter D_{eq} according to Rayleigh (blue), Mie (solid) and T-Matrix (dashed) theory. While the effective reflectivity derived with Rayleigh theory increases with the square of the particle mass, Z_e starts to deviate for Mie and T-Matrix theory for $D_{eq} > 400\,\mu m$m at 94 GHz and for $D_{eq} > 800\,\mu m$ at 35 GHz. For D_{eq} larger than $600\,\mu m$ ($1200\,\mu m$), effective reflectivity for single ice spheroids decreases again for 94 GHz (resp. 35 GHz) due to Mie resonances. The reader is advised that the results in Fig. 9a probably underestimate the backscatter for snowflakes at larger D_{eq} (Tyynelä et al., 2011).

In a next step, this result is integrated using the normalized PSDs for different effective radii. The results for a fixed ice water content of $1\,\mathrm{gm}^{-1}$ and variable effective ice crystal radius is shown in Fig. 9b.
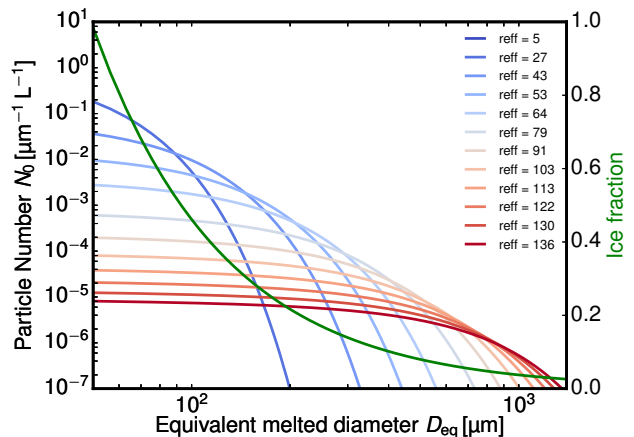
Figure 8. The ice microphysical model used during the effective reflectivity study. The particle size distribution (Delanoë et al., 2005) and the mass-size relationship (green curve) (Heymsfield et al., 2010) are based on an extensive database of airborne in situ measurements.

Lower effective reflectivity values are almost identical, while larger effective reflectivities at 94 GHz are below the values at 35 GHz. For these realistic PSDs, effective reflectivities deviate from Rayleigh theory for effective radii larger than $80\,\mu m$ at 94 GHz and $120\,\mu m$ at 35 GHz. In Fig. 9b, the non-Rayleigh scattering effects become apparent at much smaller values of r_{eff} compared to values of D_{eq} in Fig. 9a. This is only an apparent contradiction, since r_{eff} increases proportional to the ratio of mass to projected area ratio and thereby much slower than D_{eq}.

At last, the PSD-integrated results from Fig. 9b are used to constrain co-located Z_e measurements at 35 GHz and 94 GHz to physically plausible values. In Fig. 10, modeled effective reflectivities at 94 GHz are plotted against reflectivities at 35 GHz. The blue lines show the Rayleigh result, the solid lines show result according to Mie theory and the dashed lines show results for spheroids which where obtained from T-Matrix theory. Fig. 10a shows results for mono-disperse ice particles with increasing D_{eq}, while Fig. 10b shows results for whole ice crystal distributions with increasing r_{eff} and a fixed ice water content of $1\,\mathrm{gm}^{-1}$. Obviously, Z_e values measured at 94 GHz should always be equal or smaller than Z_e values measured at 35 GHz. While Z_e can also be much smaller due to the combination of non-Rayleigh scattering and higher attenuation at 94 GHz, ice clouds with smaller ice crystals and thus effective reflectivity should exhibit quite similar Z_e values at 94 and 35 GHz.

5.2 RASTA

The calibration of the 94 GHz Doppler cloud radar named RASTA on board the French Falcon 20 was performed by Protat et al. (2009) with an absolute accuracy of 1 dB by using the ocean surface backscatter. In intercomparisons,
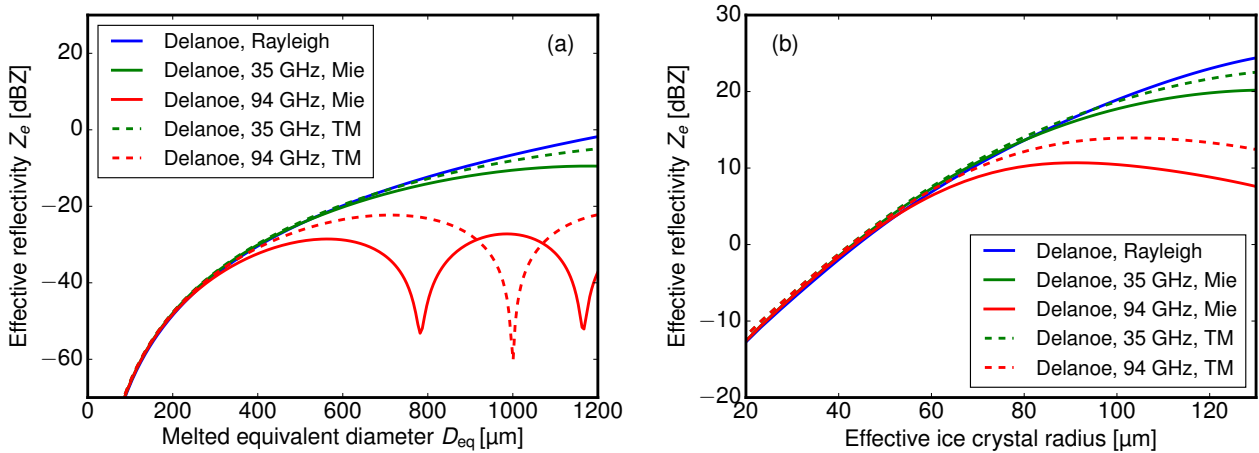
Figure 9. Modeled effective reflectivities at 35 GHz (green) and 94 GHz (red) as a function of equivalent melted diameter D_{eq} according to Rayleigh (blue), Mie (solid) and T-Matrix (dashed) theory. **(a)** Results for mono-disperse, horizontally aligned oblate spheroids with an aspect ratio of 0.6, composed of a mixture of air and ice according to Fig 8. **(b)** Results for particle size distributions (shown in Fig. 8) of these spheroids with a fixed ice water content of $1\,\mathrm{g\,m^{-1}}$.
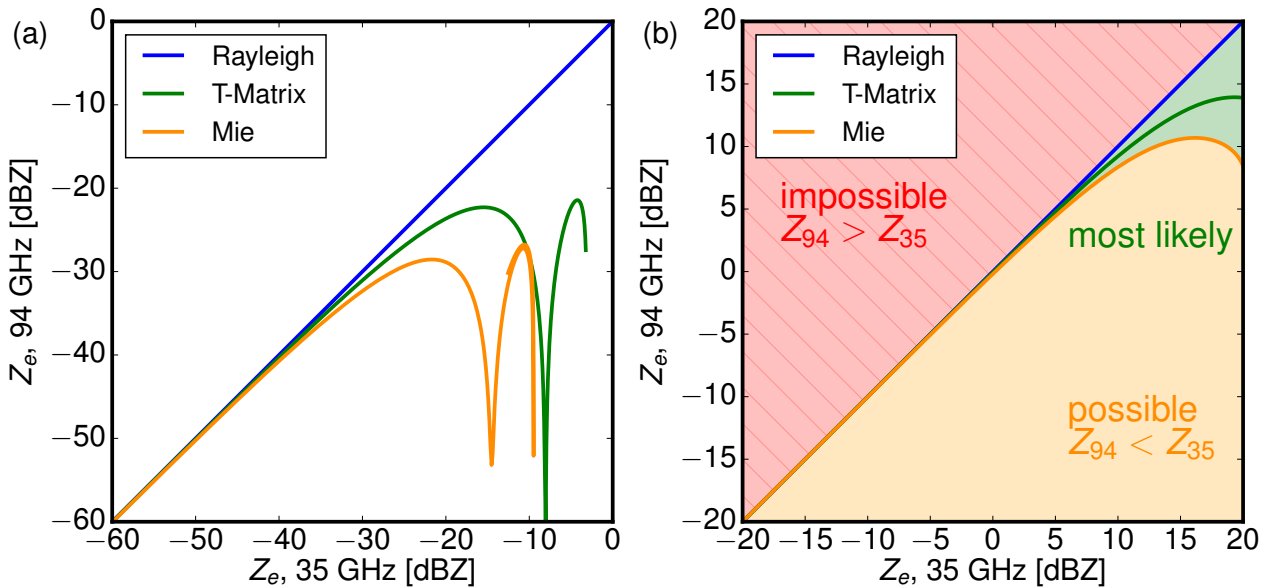
Figure 10. Comparison between modeled effective reflectivities at 94 GHz against effective reflectivities at 35 GHz according to Rayleigh (blue), Mie (solid) and T-Matrix (dashed) theory. **(a)** Z_e for mono-disperse ice crystals (soft spheroids), **(b)** Z_e for the whole distribution shown in Fig. 8. Overall, the results for both wavelengths are almost identical for small particle sizes and thus small Z_e, while Z_e at 94 GHz is smaller than at 35 GHz for larger particles and thus larger Z_e values.

they found that CloudSat measured about $1\,\mathrm{dB}$ higher reflectivities compared to RASTA. A coordinated flight with the French Falcon equipped with the 94 GHz radar system RASTA and the HALO equipped with the 35 GHz radar system was performed on over Southern France and Northern Spain on 19 December 2013 between 11:00 and 11:15 UTC. Both aircraft flew in close separation of less than 5 minutes. During that leg, HALO was flying at an altitude of $13\,\mathrm{km}$ and passed the slower flying French FALCON at an altitude

of $10\,\mathrm{km}$. The SEVIRI satellite image indicated a stratiform cloud in the measurement area (Fig. 11).

The radar measurements showed a two layer cloud structure (Fig. 12) with a lower cloud in the first half of the measurement reaching from ground to about $4\,\mathrm{km}$ height and an overlying cloud layer, present during the whole co-located flight, with a cloud base between about $4.5\,\mathrm{km}$ and $6\,\mathrm{km}$ height and an homogeneous cloud top at about $10.5\,\mathrm{km}$ in altitude. Thus, this coordinated flight provides an optimal measurement situation for a radar inter-comparison. Due to the
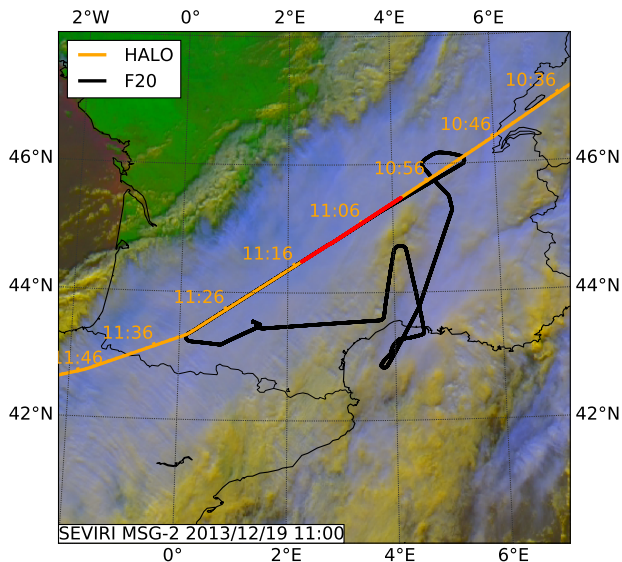
Figure 11. SEVIRI satellite image for the coordinate flight leg between HALO and the French Falcon on 19 December 2013. The intercomparison between HAMP MIRA on HALO (orange line) and RASTA on the French Falcon (black line) was conducted over a deep ice cloud layer. The red line marks the coordinated flight leg over South France between Lyon and Toulouse.

close separation of the aircraft, many cloud features can be found in both measurements at the same place. On the first sight of the measurements one can suggest that the HAMP MIRA instrument shows more variability within the cloud layer. Also small-scale cloud structures are visible in the measurements made between 11:08 and 11:12 UTC. These cloud structures are not visible in the cross-section of the RASTA measurements. At first glance, the HAMP MIRA at $35\,\text{GHz}$ is more sensitive, especially to low-lying water clouds. While the effective reflectivities of the high cirrus cloud layer is quite similar, differences become visible in precipitating clouds, but also in non-precipitating water clouds after 11:07 UTC.

Like in Sect. 4.3, Z_e were corrected for gaseous attenuation by oxygen and water vapor using the model of Rosenkranz (1998). Profiles of pressure, temperature and humidity were taken from the ECMWF Integrated Forecasting System (IFS) model. At first glance, Z_e from both instruments look quite similar in the cirrus cloud layer when using the new calibration of HAMP MIRA. In precipitating clouds at lower altitudes, however, differences in Z_e become visible. As discussed in the previous model study, this can be explained by the difference in wavelength. With increasing ice crystal size, the transition from the Rayleigh scattering regime ($Z \approx D^6$) towards the Mie scattering regime ($Z \approx D^2$) first occurs at $94\,\text{GHz}$. The difference ΔZ between 94 and $35\,\text{GHz}$ increases with increasing Z_e due to larger ice crystals and higher attenuation at lower altitudes. In

the following intercomparison, cloud parts below $4\,\text{km}$ were thus discarded (hatched line in Fig. 12) to exclude effects caused by different attenuation or scattering regimes. Common coordinates were used as reference points to obtain reflectivity pairs from both instruments. Fig. 13a gives a closer look, where the airborne RASTA and MIRA HAMP measurements of Z_e are compared against each other like in the model study shown in Fig. 10. On average, the linear regression reveals lower reflectivities ($-1.4\,\text{dB}$) for RASTA. While slightly outside their calibration uncertainties, the agreement is still quite well with the slight time shift and wavelength difference in mind.

5.3 CloudSat

In recent years, CloudSat has been established as a reference source to compare the calibration of different ground- and airborne cloud radars (Protat et al., 2010). Due to the stability of its absolute calibration and its global coverage, CloudSat has tied the different cloud radar systems more closely together. For this reason, the spaceborne CloudSat is used in this last comparison. For intercomparison, a CloudSat underflight performed over the subtropical North-Atlantic ocean east of Barbados on 17th August 2016 between 16:54 and 17:22 UTC (Fig. 14) is used. Due to the different conventions for the dielectric factor ($|K|^2 = 0.75$ for Cloudsat, $|K|^2 = 0.93$ for HAMP MIRA) the effective reflectivity from CloudSat had first to be converted for $|K|^2 = 0.93$ using Eq. 1. Using a nearby dropsonde sounding, the two-way attenuation by water vapor and oxygen absorption was calculated at $35\,\text{GHz}$ and $94\,\text{GHz}$ and used to correct Z_e. For this underflight, Fig. 14a shows a corresponding image of the scene at a wavelength of $645\,\text{nm}$ which was acquired by the Wide Field Camera (Pitts, 2007) on CALIPSO. HALO flew aligned with the CloudSat footprint for over $450\,\text{km}$. During this flight, all instrument settings were identical to the calibration flight ($f_p = 6\,\text{kHz}$, $\tau = 200\,\text{ns}$, $1\,\text{Hz}$) with footprints measuring approximately $100\,\text{m}$ in the horizontal and $30\,\text{m}$ in the vertical. In the beginning of the underpass flight, HALO was still climbing through the cirrus layer. Coinciding with the CloudSat overpass at 17:04 UTC, the aircraft then reached the top of the cirrus layer. The overall measurement scene is characterized by inhomogeneous cirrus cloud structures with contribution of few low clouds. The first part is dominated by an extended cirrus layer. As this cirrus layer becomes thinner, the second part is composed of broken and thinner cirrus clouds and shallow, convective marine boundary layer clouds. The cirrus layer as well as the lower precipitating clouds are clearly visible from both platforms. Strong effective reflectivity gradients are more blurred in the CloudSat measurement due to the coarser horizontal ($1700\,\text{m}$ vs $200\,\text{m}$) and vertical ($500\,\text{m}$ vs $30\,\text{m}$) resolution. For this reason, cloud edges as well as internal cloud structures are better resolved in the HAMP MIRA measurements. At cloud edges, this resolution induced blurring leads to larger reflec-
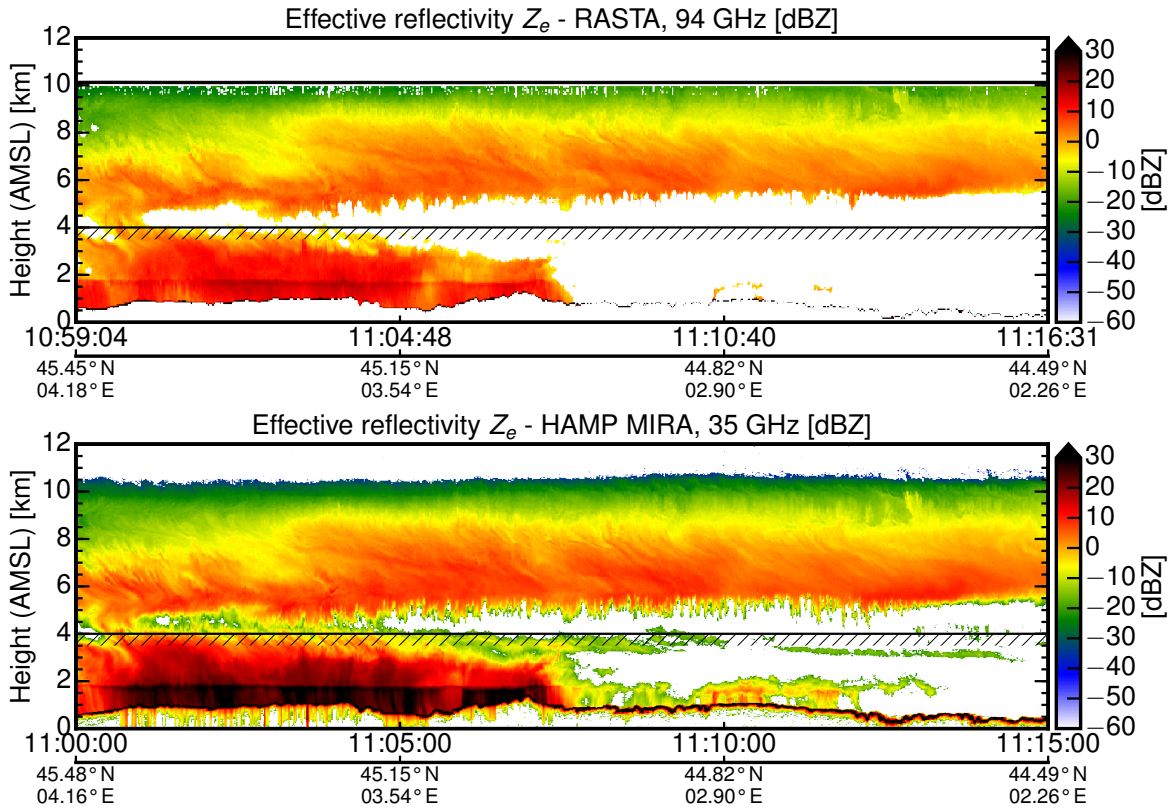
Figure 12. Radar measurements performed with RASTA at $94\,\mathrm{GHz}$ (upper panel) and HAMP MIRA at $35\,\mathrm{GHz}$ (lower panel) along the coordinated flight track marked in Fig. 11. The reflectivity of HAMP MIRA was calculated using the new calibration. Cloud parts below $4\,\mathrm{km}$ (hatched line) were discarded in the direct comparison of Z_e values in Fig. 13a to exclude effects caused by different attenuation or scattering regimes. The thin black line between 0.5 and $1.5\,\mathrm{km}$ shows the ground return of the *Massif Central*

.

tivities while it reduces the maximum reflectivities found inside clouds. For the direct comparison in Fig. 13b, cloud parts below $4\,\mathrm{km}$ are again discarded (hatched line in Fig. 14) to exclude effects caused by different attenuation or scattering regimes. Again, common coordinates were used as reference points to obtain reflectivity pairs from both instruments. Since the scene is dominated by cirrus, the values for Z_e are generally lower than in the RASTA-MIRA comparison. In contrast to the RASTA comparison, the linear regression reveals slightly larger reflectivities ($+1.0\,\mathrm{dB}$) for CloudSat. In comparison to Fig. 13a, the scatter between air- and spaceborne platform is significantly larger due to the different spatial resolutions and instrument footprints. The small bias between CloudSat and HAMP MIRA is however within the calibration uncertainties of both instruments. The fact that the effective reflectivity measured by HAMP MIRA is in between RASTA and CloudSat serves as further validation of the new absolute calibration.

6   Conclusions

In this study, we have characterized the absolute calibration of the microwave cloud radar *HAMP MIRA*, which is installed in the belly pod section of the German research aircraft *HALO* in a fixed nadir-pointing configuration. In a first step, the respective instrument components were characterized in the laboratory to obtain an internal calibration of the instrument. Our study confirmed the previously assumed antenna gain and the linearity of the receiver:

- The antenna gain $G_a = 50.0\,\mathrm{dBi}$ and beam pattern ($-3\,\mathrm{dB}$ beamwidth $\phi = 0.56\,°$) showed no obvious asymmetries or increased sidelobes.

- With three attenuator settings ($0/15/30\,\mathrm{dB}$), the radar receiver behaved very linear ($m = 1.0009$ and residual $0.054\,\mathrm{dB}$) in a wide dynamic range of $70\,\mathrm{dB}$ from $-105\,\mathrm{dBm}$ to $-5\,\mathrm{dBm}$.
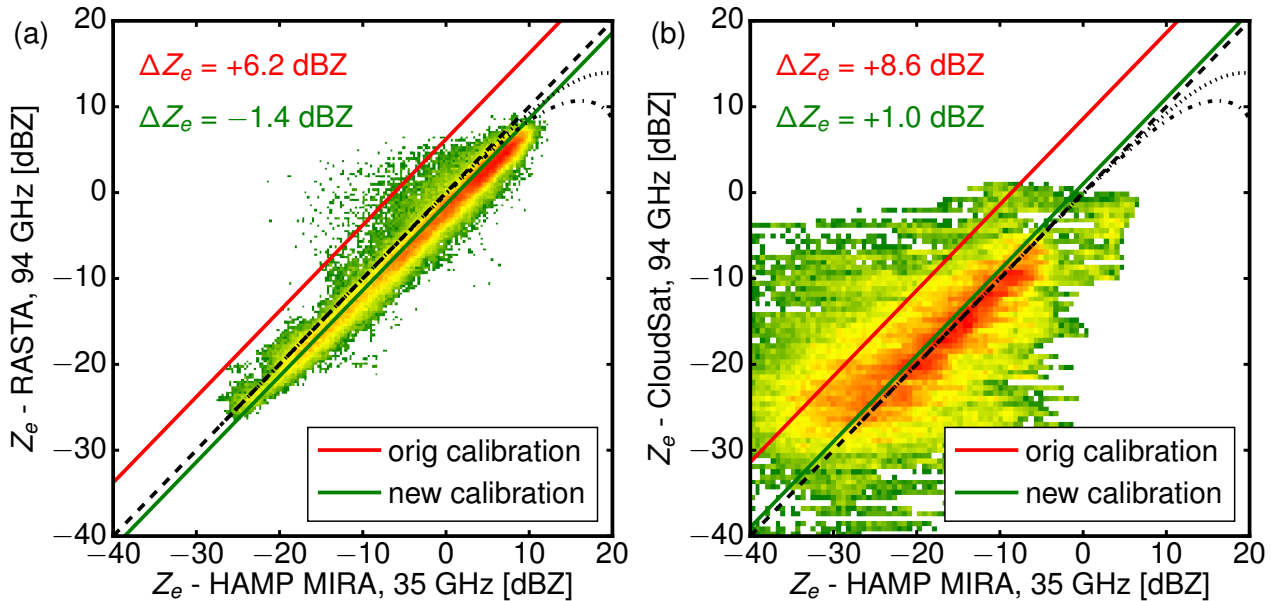
Figure 13. (a) Comparison of effective reflectivities shown in Fig. 12 measured with HAMP MIRA at $35\,\text{GHz}$ and the airborne RASTA instrument at $94\,\text{GHz}$. **(b)** Comparison of effective reflectivities shown in Fig. 14 measured with HAMP MIRA at $35\,\text{GHz}$ and the spaceborne CloudSat instrument at $94\,\text{GHz}$. In both cases, common coordinates were used as reference points to obtain reflectivity pairs from both instruments. The green line shows the offset fit for the new, the red line for the old HAMP MIRA calibration. The linear regression reveals lower reflectivities ($-1.4\,\text{dB}$) for RASTA but slightly higher reflectivities ($+1.0\,\text{dB}$) for CloudSat.

– No further saturation by additional receiver components (e.g. mixers or filters) could be detected up to an input power of $-5\,\text{dBm}$. This allows to shift the dynamic range by using the attenuator to measure higher input powers (which would otherwise be saturated) without losing the absolute calibration.

A key component of this work was the characterization of the spectral response of the radar receiver and its power transfer function $\mathcal{T}$ using an analog continuous wave signal generator. This characterization gave valuable new insights about the receiver noise power and thus the receiver sensitivity. In the course of this study, following major improvements to the instrument calibration were made:

– The comparison of the measured and the previously estimated total receiver noise power ($-95.3\,\text{dBm}$ vs. $-98.2\,\text{dBm}$) revealed an underestimation of $2.9\,\text{dB}$.

– This underestimation of P_n could be traced back to two different origins within the radar receiver

– Spectral response measurements of the receiver unveiled a larger receiver noise bandwidth of $7.5\,\text{MHz}$, compared to the $5.0\,\text{MHz}$ expected by the used matched filter ($\tau_r = 200\,\text{ns}$). This issue could be traced back to an additional window function which was applied unintentionally to IQ data within the digital signal processor. The larger receiver response led to a bit higher thermal noise power P_{kTB} ($-106.9\,\text{dBm}$ vs. $-105.2\,\text{dBm}$) than initially assumed.

– The noise figure NF, describing the additional noise created by the receiver itself, turned out to be $1.1\,\text{dB}$ larger than previously estimated, but showed no dependence on τ_r.

– The combination of a larger spectral response ($1.8\,\text{dB}$) and higher noise figure ($1.1\,\text{dB}$) caused the $2.9\,\text{dB}$ underestimation of the inherent noise power P_n. This, in turn, lead to an $2.9\,\text{dB}$ underestimation of Z_e.

– Furthermore, no correction of the finite receiver bandwidth loss was applied to previous data sets of HAMP MIRA. Using the spectral response measurements, this study can now give an estimate for the finite receiver bandwidth loss L_{fb} of $1.2\,\text{dB}$.

In addition, our study re-evaluated the previously assumed attenuation by the belly pod and additional waveguides with measurements:

– The thickness of the epoxy quartz radome in the belly pod was designed with a thickness of $4.53\,\text{mm}$ to limit the one-way attenuation to around $0.5\,\text{dB}$. Deviations during manufacturing increased the planned belly pod thickness from $4.53\,\text{mm}$ to $4.84\,\text{mm}$. This increased the one-way attenuation from initially assumed $0.5\,\text{dB}$ to $1.5\,\text{dB}$. The higher radome attenuation is now also confirmed by laboratory measurements.

– The initially used calibration did not accounted for the losses caused by the longer waveguides in the airplane
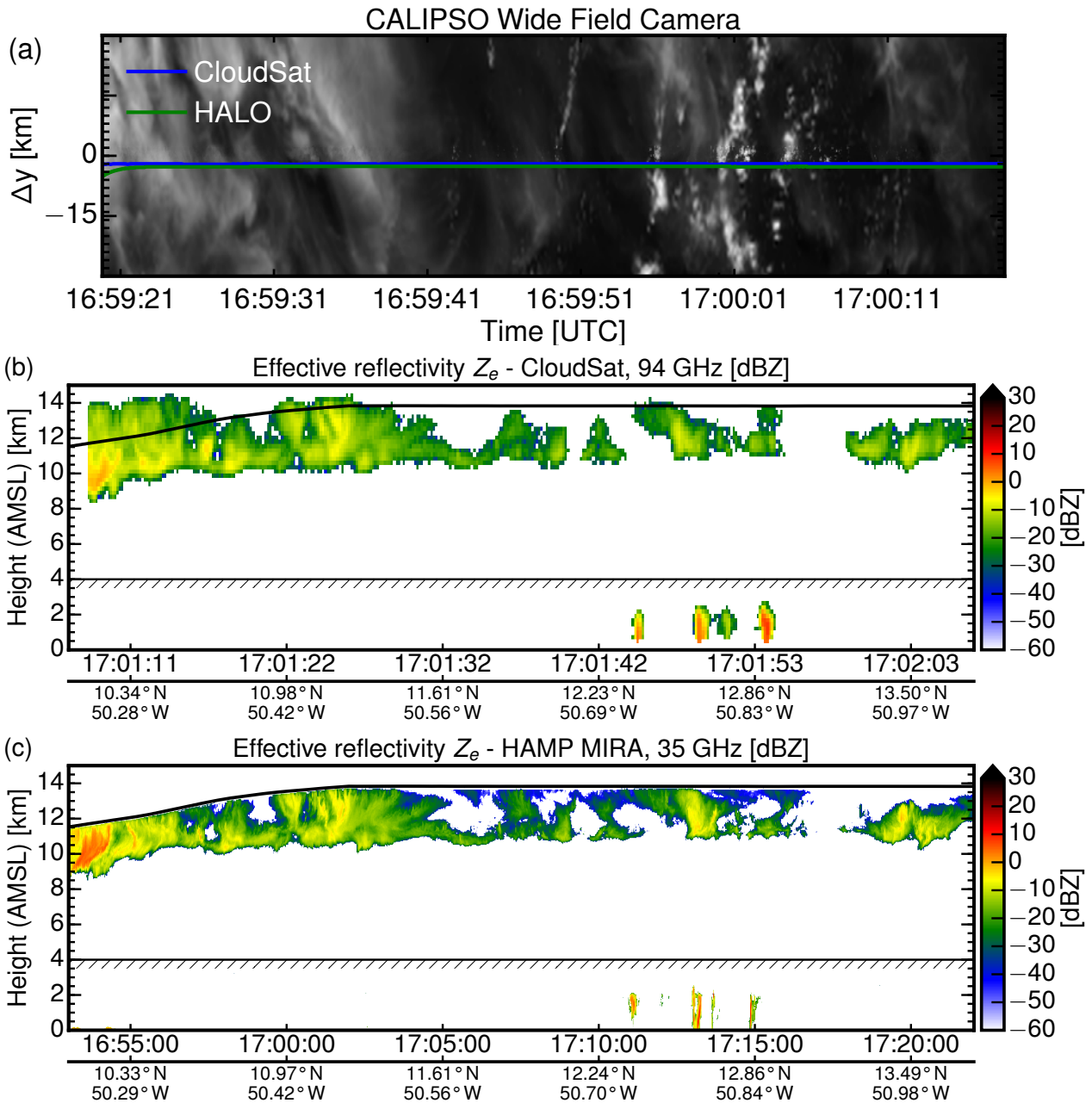
Figure 14. CloudSat underflight performed with HALO over the subtropical North-Atlantic ocean east of Barbados on 17th August 2016. **(a)** Corresponding image along the common flight path which was acquired by the Wide Field Camera on CALIPSO. **(b)** Equivalent effective reflectivity Z_e measured by the spaceborne CloudSat radar at 94 GHz and **(c)** by HAMP MIRA at 35 GHz. Again, cloud parts below 4 km (hatched line) were discarded in the direct comparison of Z_e values in Fig. 13b.

installation. With an additional length of $1.15\,\mathrm{m}$ and a specified attenuation of $0.65\,\mathrm{dB/m}$, the two-way attenuation by additional waveguides is $1.5\,\mathrm{dB}$.

Subsequently, this component calibration was validated by using the ocean surface backscatter as a reference with known reflectivity. To this end, controlled roll maneuvers were flown during the NARVAL2 campaign in the vicinity of Barbados to sample the angular dependence of the ocean surface backscatter. The comparison with modeled backscatter values using the Cox-Munk model for non-slick ocean surfaces and measured values from the GPM satellite confirmed the internal calibration to within $\pm 0.5\,\mathrm{dB}$. In a second intercomparison study, the absolute accuracy of the internal calibration was further scrutinized during common flight legs with the airborne $94\,\mathrm{GHz}$ cloud radar RASTA and the spaceborne $94\,\mathrm{GHz}$ cloud radar CloudSat. To asses the influence of different radar wavelengths on this comparison, we first conducted a model study of effective reflectivities at 35 and $94\,\mathrm{GHz}$. Using realistic ice particle size distributions, T-Matrix calculations for spheroids show almost identical effective reflectivities at 35 and $94\,\mathrm{GHz}$ for effective radii smaller than $50\,\mu\mathrm{m}$. Larger ice crystals and higher attenuation generally lead to a smaller reflectivity at $94\,\mathrm{GHz}$. In this context, the intercomparison showed good agreement between the *HAMP MIRA* at 35 and the RASTA at $94\,\mathrm{GHz}$ with slightly lower reflectivities ($-1.3\,\mathrm{dB}$) for RASTA. The intercomparison with CloudSat showed slightly higher ($+1.2\,\mathrm{dB}$) reflectivities for CloudSat. These higher reflectivities were mostly found at cloud edges where the coarser spatial resolution of CloudSat can blur out higher reflectivities into regions with thinner reflectivity below the sensitivity of CloudSat. The intercomparison studies showed that the absolute calibration uncertainty is now well below the initially required accuracy of $3\,\mathrm{dB}$ and even brought close to the target accuracy of $1\,\mathrm{dB}$.

In conclusion, following procedures and techniques turned out to be essential for the absolute calibration of HAMP MIRA and should become state of the art:

1. The simultaneous characterization of the spectral response of the radar receiver and its power transfer function $\mathcal{T}$ turned out to be very valuable to cross-check the receiver sensitivity P_n.

2. While P_n was previously estimated using an assumed receiver noise bandwidth B and a measured receiver noise factor F_n, it is now measured directly using a calibrated signal generator with adjustable power output.

3. Moreover, the signal generator should offer a frequency sweep mode to determine the spectral response to measure the receiver noise bandwidth B. A characterized spectral response is essential to calculate the finite receiver bandwidth loss L_{fb}. It can also be used to calculate the receiver sensitivity P_n.

4. The direct measurement of P_n and the calculated value can then be used to evaluate and check the receiver noise factor F_n. This should be done for two different matched filter lengths to characterize the dependence of B_n and F_n on τ_r.

5. Discrepancies between the component-wise calculation of P_n and the direct measurement can help to find additional noise sources or attenuation within the radar receiver.

6. Validate the budget approach of the internal calibration in intercomparison with external sources like seasurface or different instruments

The lessons learned in the course of this study helped us to better understand our instrument and increased the confidence in its absolute calibration. Subsequent studies for similar cloud radar instruments should consider following prerequisites and guidelines:

– Knowledge about existing calibration offsets grows gradually. It is advisable to refrain from incremental updates of prior data sets. To mitigate confusion with different calibration offsets, a new calibration should only be applied to prior or current measurements when the internal calibration is in agreement with external reference sources.

– Initially, the main focus should be on the antenna gain (including the radome) and the receiver sensitivity. The measured antenna gain and the radome attenuation should furthermore be cross checked with calculated values.

– For the characterization of the spectral response and receiver noise power, access to unprocessed Doppler spectra is advantageous to check the calculation of SNR independently.

– The sole intercomparison of two cloud radars is a necessary but not sufficient step towards an absolute calibration. An apparent agreement can lead to a false sense of accuracy since common misconceptions and assumptions remain hidden and can thus propagate from instrument to instrument. Discrepancies in intercomparisons should always trigger a re-evaluation of the internal calibration.

– While a sole internal calibration can help to get a better understanding of the instrument performance, it has to be validated with external reference sources. It is the combination of internal calibration and external validation which establishes trust in the absolute calibration.

Data availability. The recalibrated data set of *HAMP MIRA* is available in ESSD with the identifier https://doi.org/10.5194/

essd-2018-116. The data set is described in detail in Konow et al. (2018). All data sets created during the internal calibration are provided upon request.

Appendix A: Temperature dependence of I_mg and $\langle P_t \rangle$

In-flight thermistor measurements of the average transmit power $\langle P_t \rangle$ proved to be unreliable due to strong variations in ambient temperatures in the cabin. For this reason, thermally controlled measurements of $\langle P_t \rangle$ were conducted on ground which were correlated with measured magnetron currents I_m. The relationship between both parameters then allowed to derive $\langle P_t \rangle$ from in-flight measurements of I_m. For this analysis, we operated the HAMP MIRA instrument within a trailer during a 27-day ground-based test campaign in 2016. We observed the magnetron temperature T_mg and the magnetron anode current I_mg for two different anode voltages (15.4 kV and 15.5 kV). The average transmit power $\langle P_t \rangle$ was measured every 30 min using a calibrated thermistor. Fig. A1a shows the relationship between magnetron temperature T_mg and magnetron anode current I_mg. The relationship between magnetron anode current I_mg and average transmit power $\langle P_t \rangle$ is given in Fig. A1b. Depending on the anode voltage, $\langle P_t \rangle$ increased linearly with I_mg and varied by 0.2 dB within the operational range of T_mg between $25°C$ and $35°C$.

Appendix B: Characterization of the belly pod transmission

The thickness of the epoxy quartz radome in the belly pod was designed with a thickness d of 4.53 mm to limit the one-way attenuation to around 0.5 dB. The thickness was designed to cancel out reflections on the front and back side of the radome. However, laboratory measurements of the finished radome found a one-way attenuation of around 1.5 dB for the transmit frequency 35.5 GHz of HAMP MIRA. The spectral transmission of the radome between 26 GHz and 40 GHz is shown in Fig. B1a. The red line shows the initially assumed spectral transmission using a relative permittivity $\epsilon_r = 3.44$, a dielectric loss tangent $\tan \delta = 0.0015$ and a radome thickness $d = 4.53$ mm. Our measurements (black crosses), however, can be better explained by the green line in Fig. B1a, which shows the spectral transmission for a relative permittivity $\epsilon_r = 3.80$, a dielectric loss tangent $\tan \delta = 0.0017$ and a radome thickness $d = 4.84$ mm. In Fig. B1b, the transmission for both material properties are compared as a function of the radome thickness d. The oscillating transmission can be explained by the cancellation of reflections at every half-wavelength. Since the wavelength is shorter within the radome material ($\epsilon_r = 3.80$), this happens every $d_\mathrm{opt} = \lambda / (2\sqrt{\epsilon_r}) = 2.2$ mm at 35.5 GHz. The combination of a higher relative permitivitty and the slight increase in

radome thickness can explain the 1 dB increase in radome attenuation.

Author contributions. FE and MB conceived the concept for the internal calibration. FE, MB, MH and LH performed the internal calibration and the airborne measurements. FE developed the presented methods and carried out the analysis. FE, MB and MH contributed to the interpretation of the results. JD provided the single scattering results and RASTA measurements. FE took the lead in writing the manuscript. All authors provided feedback on the manuscript.

Competing interests. The authors declare no conflict of interest.

Acknowledgements. This work was jointly supported by the German Aerospace Center (DLR), the Max Planck Society (MPI) and the German Research Foundation (DFG) through the HALO Priority Program SPP 1294, *Atmospheric and Earth System Research with the Research Aircraft HALO (High Altitude and Long Range Research Aircraft)*. Measurement equipment was kindly provided by DLR-HR. DLR-FX and its pilots are thanked for their great support during research flights. GPM data was provided by the NASA/Goddard Space Flight Center's PPS team, which develop and compute the *GPM DPR Ka vertical profile precipitation swath retrievals* (DOI: 10.5067/GPM/DPR/Ka/2A/04) as a contribution to GPM. The authors thank Oliver Lux for his internal review of the manuscript.

References

Acquistapace, C., Kneifel, S., Löhnert, U., Kollias, P., Maahn, M., and Bauer-Pfundstein, M.: Optimizing observations of drizzle onset with millimeter-wavelength radars, Atmos. Meas. Tech., 10, 1783–1802, https://doi.org/10.5194/amt-10-1783-2017, https://www.atmos-meas-tech.net/10/1783/2017/, 2017.

Agilent Technologies, Noise Figure Measurement Accuracy — The Y-Factor Method, Application Note 57-2, Oct. 2004.

Apel, J. R.: An improved model of the ocean surface wave vector spectrum and its effects on radar backscatter, Journal of Geophysical Research: Oceans, 99, 16 269–16 291, https://doi.org/10.1029/94JC00846, http://onlinelibrary.wiley.com/doi/10.1029/94JC00846/abstract, 1994.

Atlas, D.: Radar Calibration: Some Simple Approaches, Bulletin of the American Meteorological Society, 83, 1313–1316, https://doi.org/10.1175/1520-0477(2002)083<1313:RCSSA>2.3.CO;2, https://journals.ametsoc.org/doi/abs/10.1175/1520-0477(2002)083%3C1313:RCSSA%3E2.3.CO;2, 2002.

Barrick, D. E., Headrick, J. M., Bogle, R. W., and Crombie, D. D.: Sea backscatter at HF: Interpretation and utilization of the echo, Proceedings of the IEEE, 62, 673–680, https://doi.org/10.1109/PROC.1974.9507, 1974.

Bauer-Pfundstein, M. and Görsdorf, U.: Target separation and classification using cloud radar Doppler-spectra, in: Proceedings 33rd Intern. Conf. on Radar Meteorology, Cairns, http://ams.
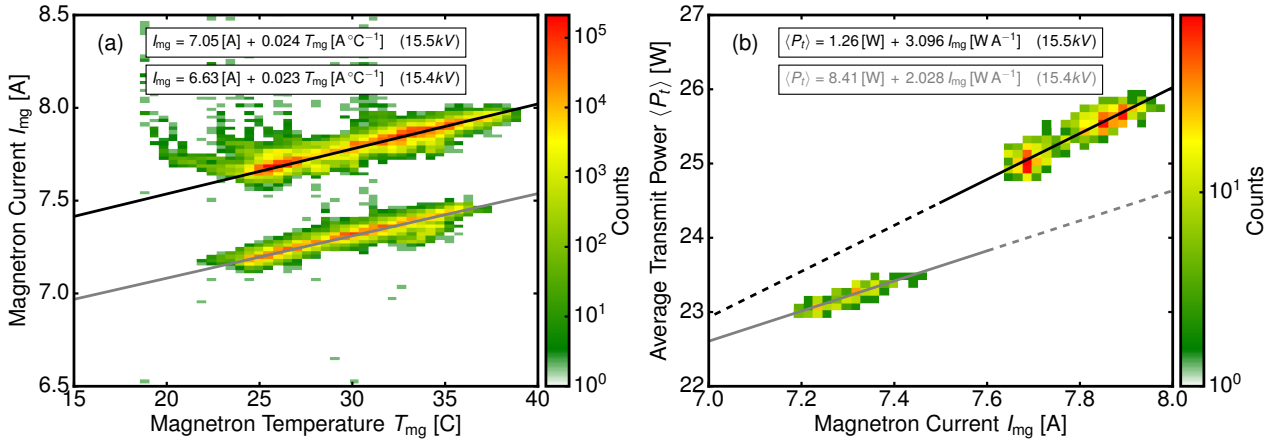
Figure A1. Analysis of the relationship between magnetron temperature T_{mg}, magnetron anode current I_{mg} and average transmit power $\langle P_t \rangle$ during a 27-day ground-based test campaign in 2016 for two different anode voltages (15.4 kV and 15.5 kV). **(a)** Relationship between magnetron temperature T_{mg} and magnetron anode current I_{mg}. **(b)** Relationship between magnetron anode current I_{mg} and average transmit power $\langle P_t \rangle$.
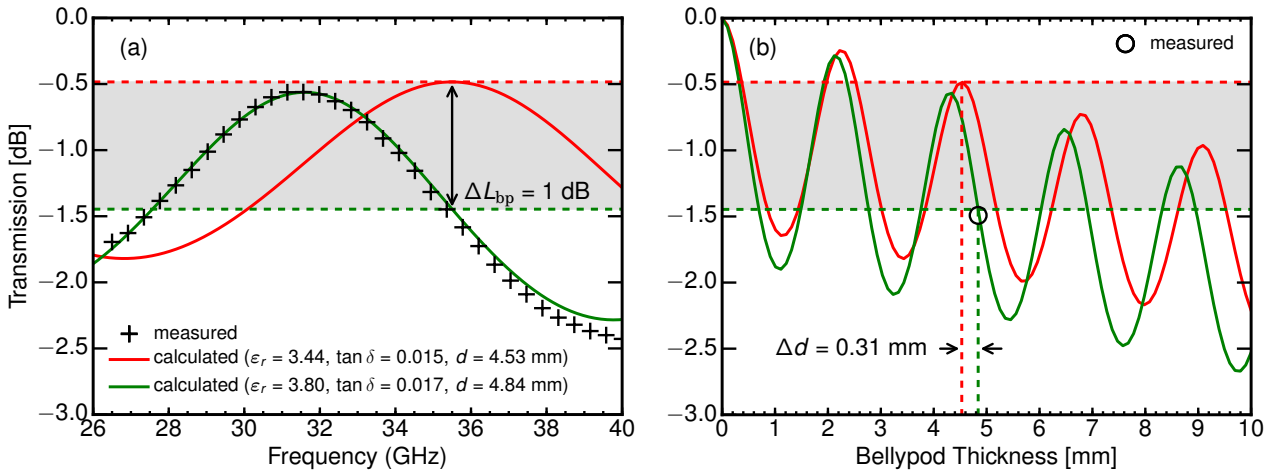
Figure B1. Analysis of the belly pod radome transmission of HALO. **(a)** Radome transmission between 26 GHz and 40 GHz for the initially assumed material properties (red line, $\epsilon_r = 3.44$, $\tan \delta = 0.0015$, $d = 4.53$ mm) and the measured ones (red line, $\epsilon_r = 3.80$, $\tan \delta = 0.0017$, $d = 4.84$ mm). **(b)** Radome transmission for the two material properties (red: assumed, green: measured) as a function of the radome thickness d. A increase in relative permittivity and thickness ($\Delta = 0.31$ mm) increased the radome attenuation by 1 dB.

confex.com/ams/33Radar/techprogram/paper_123456.htm, 2007.

Bormotov, V., Peters, G., Schünemann, K., Vavriv, D., Vinogradov, V., and Volkov, V.: 36 GHz Doppler radar for remote sensing of the atmosphere, in: Proceedings of Millennium Conference on Antenna and Propagation, Davos Switzerland, pp. 9–14, 2000.

Boucher, O., Randall, D., Artaxo, P., Bretherton, C., Feingold, G., Forster, P., Kerminen, V.-M., Kondo, Y., Liao, H., Lohmann, U., Rasch, P., Satheesh, S., Sherwood, S., Stevens, B., and Zhang, X.: Clouds and Aerosols, book section 7, pp. 571–658, Cambridge University Press, Cambridge, United Kingdom and New York, NY, USA, https://doi.org/10.1017/CBO9781107415324.016, www.climatechange2013.org, 2013.

Bouniol, D., Protat, A., Plana-Fattori, A., Giraud, M., Vinson, J.-P., and Grand, N.: Comparison of Airborne and Spaceborne 95-GHz Radar Reflectivities and Evaluation of Multiple Scattering Effects in Spaceborne Measurements, Journal of Atmospheric and Oceanic Technology, 25, 1983–1995, https://doi.org/10.1175/2008JTECHA1011.1, http://journals.ametsoc.org/doi/abs/10.1175/2008JTECHA1011.1, 2008.

Brown, G. S.: Quasi-Specular Scattering from the Air-Sea Interface, in: Surface Waves and Fluxes, Environmental Fluid Mechanics, pp. 1–39, Springer, Dordrecht, https://link.springer.com/chapter/10.1007/978-94-009-0627-3_1, dOI: 10.1007/978-94-009-0627-3_1, 1990.

Caylor, I. J., Heymsfield, G. M., Meneghini, R., and Miller, L. S.: Correction of Sampling Errors in Ocean Surface Cross-Sectional Estimates from Nadir-Looking Weather Radar, Journal of Atmospheric and Oceanic Technology, 14, 203–210, https://doi.org/10.1175/1520-0426(1997)014<0203:COSEIO>2.0.CO;2, http://journals.ametsoc.org/doi/full/10.1175/1520-0426(1997)014%3C0203%3ACOSEIO%3E2.0.CO%3B2, 1997.

Caylor, I. J. H.: NASA ER-2 Doppler radar reflectivity calibration for the CAMEX project, Tech. rep., Goddard Space Flight Center. Greenbelt, Maryland, https://ntrs.nasa.gov/search.jsp?R=19940033279, 1994.

Chandrasekar, V., Baldini, L., Bharadwaj, N., and Smith, P. L.: Calibration procedures for global precipitation-measurement ground-validation radars, URSI Radio Science Bulletin, 355, 45–73, 2015.

Chen, T., Zhang, Y., and Rossow, W.: Sensitivity of atmospheric radiative heating rate profiles to variations of cloud layer overlap, Journal of Climate, 13, 2941–2959, 2000.

Cox, C. and Munk, W.: Measurement of the roughness of the sea surface from photographs of the sun's glitter, Journal of the Optical Society of America, 44, 838–850, 1954.

Delanoë, J., Protat, A., Testud, J., Bouniol, D., Heymsfield, A. J., Bansemer, A., Brown, P. R. A., and Forbes, R. M.: Statistical properties of the normalized ice particle size distribution, Journal of Geophysical Research: Atmospheres, 110, D10 201, https://doi.org/10.1029/2004JD005405, http://onlinelibrary.wiley.com/doi/10.1029/2004JD005405/abstract, 2005.

Delanoë, J. and Hogan, R. J.: A variational scheme for retrieving ice cloud properties from combined radar, lidar, and infrared radiometer, Journal of Geophysical Research, 113, D07 204, http://www.agu.org/pubs/crossref/2008/2007JD009000.shtml, 2008.

Delanoë, J. M. E., Heymsfield, A. J., Protat, A., Bansemer, A., and Hogan, R. J.: Normalized particle size distribution for remote sensing application, Journal of Geophysical Research: Atmospheres, 119, 4204–4227, https://doi.org/10.1002/2013JD020700, http://onlinelibrary.wiley.com/doi/10.1002/2013JD020700/abstract, 2014.

Deng, M., Mace, G. G., Wang, Z., and Okamoto, H.: Tropical Composition, Cloud and Climate Coupling Experiment validation for cirrus cloud profiling retrieval using CloudSat radar and CALIPSO lidar, Journal of Geophysical Research: Atmospheres, 115, D00J15, https://doi.org/10.1029/2009JD013104, http://onlinelibrary.wiley.com/doi/10.1029/2009JD013104/abstract, 2010.

Donovan, D. P., van Lammeren, A., Hogan, R., Russchenberg, H., Apituley, A., Francis, P., Testud, J., Pelon, J., Quante, M., and Agnew, J.: Combined radar and lidar cloud remote sensing: Comparison with IR radiometer and in-situ measurements, Phys. Chem. Earth (B), 25, 1049–1055, 2000.

Doviak, R. J. and Zrnić, D.: Receiver Bandwidth Effect on Reflectivity and Doppler Velocity Estimates, Journal of Applied Meteorology, 18, 69–76, https://doi.org/10.1175/1520-0450(1979)018<0069:RBEORA>2.0.CO;2, http://journals.ametsoc.org/doi/abs/10.1175/1520-0450%281979%29018%3C0069%3ARBEORA%3E2.0.CO%3B2, 1979.

Doviak, R. J. and Zrnić, D. S.: Doppler Radar and Weather Observations, Dover Publications, 1993.

Durden, S. L., Im, E., Li, F. K., Ricketts, W., Tanner, A., and Wilson, W.: ARMAR: An Airborne Rain-Mapping Radar, Journal of Atmospheric and Oceanic Technology, 11, 727–737, https://doi.org/10.1175/1520-0426(1994)011<0727:AAARMR>2.0.CO;2, http://journals.ametsoc.org/doi/abs/10.1175/1520-0426%281994%29011%3C0727%3AAAAARMR%3E2.0.CO%3B2, 1994.

Ewald, F., Winkler, C., and Zinner, T.: Reconstruction of cloud geometry using a scanning cloud radar, Atmos. Meas. Tech., 8, 2491–2508, https://doi.org/10.5194/amt-8-2491-2015, http://www.atmos-meas-tech.net/8/2491/2015/, 2015.

Freilich, M. H. and Vanhoff, B. A.: The Relationship between Winds, Surface Roughness, and Radar Backscatter at Low Incidence Angles from TRMM Precipitation Radar Measurements, Journal of Atmospheric and Oceanic Technology, 20, 549–562, https://doi.org/10.1175/1520-0426(2003)20<549:TRBWSR>2.0.CO;2, http://journals.ametsoc.org/doi/abs/10.1175/1520-0426%282003%2920%3C549%3ATRBWSR%3E2.0.CO%3B2, 2003.

Foot, J. S.: Some observations of the optical properties of clouds. II: Cirrus, Quarterly Journal of the Royal Meteorological Society, 114(479), 145–164, 1988.

Görsdorf, U., Lehmann, V., Bauer-Pfundstein, M., Peters, G., Vavriv, D., Vinogradov, V., and Volkov, V.: A 35-GHz Polarimetric Doppler Radar for Long-Term Observations of Cloud Parameters—Description of System and Data Processing, Journal of Atmospheric and Oceanic Technology, 32, 675–690, https://doi.org/10.1175/JTECH-D-14-00066.1, http://journals.ametsoc.org/doi/abs/10.1175/JTECH-D-14-00066.1, 2015.

Haimov, S. and Rodi, A.: Fixed-Antenna Pointing-Angle Calibration of Airborne Doppler Cloud Radar, Journal of Atmospheric and Oceanic Technology, 30, 2320–

2335, https://doi.org/10.1175/JTECH-D-12-00262.1, http://journals.ametsoc.org/doi/abs/10.1175/JTECH-D-12-00262.1, 2013.

Handwerker, J. and Miller, M. A.: Intercomparison of measurements obtained by vertically pointing collocated 95 GHz and 35.5 GHz cloud radars, in: Proc. Fifth European Conference on Radar in Meteorology and Hydrology, http://pd95b2c0f.dip0.t-ipconnect.de/literature/erad2008-Handwerker_35-95_ext.pdf, 2008.

Hennemuth, B., Weiss, A., Bösenberg, J., Jacob, D., Linné, H., Peters, G., and Pfeifer, S.: Quality assessment of water cycle parameters in REMO by radar-lidar synergy, Atmos. Chem. Phys., 8, 287–308, https://doi.org/10.5194/acp-8-287-2008, https://www.atmos-chem-phys.net/8/287/2008/, 2008.

Heymsfield, A. J., Schmitt, C., Bansemer, A., and Twohy, C. H.: Improved Representation of Ice Particle Masses Based on Observations in Natural Clouds, Journal of the Atmospheric Sciences, 67(10), 3303–3318, 2010.

Heymsfield, G. M., Bidwell, S. W., Caylor, I. J., Ameen, S., Nicholson, S., Boncyk, W., Miller, L., Vandemark, D., Racette, P. E., and Dod, L. R.: The EDOP Radar System on the High-Altitude NASA ER-2 Aircraft, Journal of Atmospheric and Oceanic Technology, 13, 795–809, https://doi.org/10.1175/1520-0426(1996)013<0795:TERSOT>2.0.CO;2, http://journals.ametsoc.org/doi/abs/10.1175/1520-0426%281996%29013%3C0795%3ATERSOT%3E2.0.CO%3B2, 1996.

Horie, H. and Takahashi, N.: External calibration method using sea surface scattering for satelliteborne W-band cloud profiling radar, in: Proc. of ISPRS, vol. 38, pp. 160–163, http://www.tric.u-tokai.ac.jp/isprscom8/tc8/TC8_CD/headline/NICT%20special%20Session%20-%202/NTS25_20100608144300.pdf, 2010.

Horie, H., Iguchi, T., Hanado, H., Kuroiwa, H., Okamoto, H., and Kumagai, H.: Development of a 95-GHz Airborne Cloud Profiling Radar (SPIDER) –Technical Aspects–, IEICE TRANSACTIONS on Communications, E83-B, 2010–2020, http://search.ieice.org/bin/summary.php?id=e83-b_9_2010&category=B&year=2000&lang=E&abst=, 2000.

Horie, H., Kuroiwa, H., and Kumagai, H.: Near nadir scattering properties at W-band frequency for the sea surface, in: IGARSS 2004. 2004 IEEE International Geoscience and Remote Sensing Symposium, vol. 3, pp. 1742–1745 vol.3, https://doi.org/10.1109/IGARSS.2004.1370669, 2004.

Hou, A. Y., Kakar, R. K., Neeck, S., Azarbarzin, A. A., Kummerow, C. D., Kojima, M., Oki, R., Nakamura, K., and Iguchi, T.: The Global Precipitation Measurement Mission, Bulletin of the American Meteorological Society, 95, 701–722, https://doi.org/10.1175/BAMS-D-13-00164.1, https://journals.ametsoc.org/doi/full/10.1175/BAMS-D-13-00164.1, 2013.

Illingworth, A. J., Hogan, R. J., O'Connor, E. J., Bouniol, D., Delanoë, J., Pelon, J., Protat, A., Brooks, M. E., Gaussiat, N., Wilson, D. R., Donovan, D. P., Baltink, H. K., van Zadelhoff, G.-J., Eastment, J. D., Goddard, J. W. F., Wrench, C. L., Haeffelin, M., Krasnov, O. A., Russchenberg, H. W. J., Piriou, J.-M., Vinit, F., Seifert, A., Tompkins, A. M., and Willén, U.: Cloudnet Continuous Evaluation of Cloud Profiles in Seven Operational Models Using Ground-Based Observations, Bulletin of the American Meteorological Society,

88, 883–898, https://doi.org/10.1175/BAMS-88-6-883, http://journals.ametsoc.org/doi/abs/10.1175/BAMS-88-6-883, 2007.

Illingworth, A. J., Barker, H. W., Beljaars, A., Ceccaldi, M., Chepfer, H., Clerbaux, N., Cole, J., Delanoë, J., Domenech, C., Donovan, D. P., Fukuda, S., Hirakata, M., Hogan, R. J., Huenerbein, A., Kollias, P., Kubota, T., Nakajima, T., Nakajima, T. Y., Nishizawa, T., Ohno, Y., Okamoto, H., Oki, R., Sato, K., Satoh, M., Shephard, M. W., Velázquez-Blázquez, A., Wandinger, U., Wehr, T., and van Zadelhoff, G.-J.: The EarthCARE Satellite: The Next Step Forward in Global Measurements of Clouds, Aerosols, Precipitation, and Radiation, Bulletin of the American Meteorological Society, 96, 1311–1332, https://doi.org/10.1175/BAMS-D-12-00227.1, http://journals.ametsoc.org/doi/abs/10.1175/BAMS-D-12-00227.1, 2014.

Intrieri, J. M., Stephens, G. L., Eberhard, W. L., and Uttal, T.: A Method for Determining Cirrus Cloud Particle Sizes Using Lidar and Radar Backscatter Technique, Journal of Applied Meteorology, 32, 1074–1082, https://doi.org/10.1175/1520-0450(1993)032<1074:AMFDCC>2.0.CO;2, http://journals.ametsoc.org/doi/abs/10.1175/1520-0450(1993)032%3C1074%3AAMFDCC%3E2.0.CO%3B2, 1993.

Jackson, F. C. W.: Sea surface mean square slope from Ku-band backscatter data, Journal of Geophysical Research, https://ntrs.nasa.gov/search.jsp?R=19920066044, 1992.

Klein, L. and Swift, C.: An improved model for the dielectric constant of sea water at microwave frequencies, IEEE Journal of Oceanic Engineering, 2, 104–111, https://doi.org/10.1109/JOE.1977.1145319, 1977.

Konow, H., Jacob, M., Ament, F., Crewell, S., Ewald, F., Hagen, M., Hirsch, L., Jansen, F., Mech, M., and Stevens, B.: A unified data set of airborne cloud remote sensing using the HALO Microwave Package (HAMP), Earth Syst. Sci. Data Discuss., https://doi.org/10.5194/essd-2018-116, in review, 2018.

Krautstrunk, M. and Giez, A.: The Transition From FALCON to HALO Era Airborne Atmospheric Research, in: Atmospheric Physics, edited by Schumann, U., Research Topics in Aerospace, pp. 609–624, Springer Berlin Heidelberg, http://link.springer.com/chapter/10.1007/978-3-642-30183-4_37, 2012.

Li, L., Heymsfield, G. M., Racette, P. E., Tian, L., and Zenker, E.: A 94-GHz Cloud Radar System on a NASA High-Altitude ER-2 Aircraft, Journal of Atmospheric and Oceanic Technology, 21, 1378–1388, https://doi.org/10.1175/1520-0426(2004)021<1378:AGCRSO>2.0.CO;2, http://journals.ametsoc.org/doi/abs/10.1175/1520-0426%282004%29021%3C1378%3AAGCRSO%3E2.0.CO%3B2, 2004.

Li, L., Heymsfield, G. M., Tian, L., and Racette, P. E.: Measurements of Ocean Surface Backscattering Using an Airborne 94-GHz Cloud Radar—Implication for Calibration of Airborne and Spaceborne W-Band Radars, Journal of Atmospheric and Oceanic Technology, 22, 1033–1045, https://doi.org/10.1175/JTECH1722.1, http://journals.ametsoc.org/doi/abs/10.1175/JTECH1722.1, 2005a.

Li, Z., Cribb, M., Chang, F.-L., Trishchenko, A., and Luo, Y.: Natural variability and sampling errors in solar radiation measurements for model validation over the Atmospheric Radiation Measurement Southern Great Plains region, Journal of Geophysical Research, 110, doi:10.1029/2004JD005 028, 2005b.

Lonitz, K., Stevens, B., Nuijens, L., Sant, V., Hirsch, L., and Seifert, A.: The Signature of Aerosols and Meteorology in Long-Term Cloud Radar Observations of Trade Wind Cumuli, Journal of the Atmospheric Sciences, 72, 4643–4659, https://doi.org/10.1175/JAS-D-14-0348.1, http://journals.ametsoc.org/doi/abs/10.1175/JAS-D-14-0348.1, 2015.

Maahn, M. and Kollias, P.: Improved Micro Rain Radar snow measurements using Doppler spectra post-processing, Atmos. Meas. Tech., 5, 2661–2673, https://doi.org/10.5194/amt-5-2661-2012, https://www.atmos-meas-tech.net/5/2661/2012/, 2012.

Masuko, H., Okamoto, K., Shimada, M., and Niwa, S.: Measurement of microwave backscattering signatures of the ocean surface using X band and Ka band airborne scatterometers, Journal of Geophysical Research: Oceans (1978–2012), 91, 13 065–13 083, https://doi.org/10.1029/JC091iC11p13065, http://onlinelibrary.wiley.com/doi/10.1029/JC091iC11p13065/abstract, 1986.

Mech, M., Orlandi, E., Crewell, S., Ament, F., Hirsch, L., Hagen, M., Peters, G., and Stevens, B.: HAMP – the microwave package on the High Altitude and LOng range research aircraft (HALO), Atmos. Meas. Tech., 7, 4539–4553, https://doi.org/10.5194/amt-7-4539-2014, http://www.atmos-meas-tech.net/7/4539/2014/, 2014.

Meissner, T. and Wentz, F. J.: The complex dielectric constant of pure and sea water from microwave satellite observations, IEEE Transactions on Geoscience and Remote Sensing, 42, 1836–1849, https://doi.org/10.1109/TGRS.2004.831888, 2004.

Myagkov, A., Seifert, P., Wandinger, U., Bauer-Pfundstein, M., and Matrosov, S. Y.: Effects of Antenna Patterns on Cloud Radar Polarimetric Measurements, Journal of Atmospheric and Oceanic Technology, 32(10), 1813–1828, 2015.

Myagkov, A., Seifert, P., Wandinger, U., Bühl, J., and Engelmann, R.: Relationship between temperature and apparent shape of pristine ice crystals derived from polarimetric cloud radar observations during the ACCEPT campaign, Atmos. Meas. Tech., 9, 3739–3754, https://doi.org/10.5194/amt-9-3739-2016, http://www.atmos-meas-tech.net/9/3739/2016/, 2016.

Nouguier, F., Mouche, A., Rascle, N., Chapron, B., and Vandemark, D.: Analysis of Dual-Frequency Ocean Backscatter Measurements at Ku- and Ka-Bands Using Near-Nadir Incidence GPM Radar Data, IEEE Geoscience and Remote Sensing Letters, 13, 1310–1314, https://doi.org/10.1109/LGRS.2016.2583198, 2016.

Pitts, M. C., Thomason, L. W., Hu, Y., and Winker, D. M.: An assessment of the on-orbit performance of the CALIPSO wide field camera, Proc. SPIE 6745, Remote Sensing of Clouds and the Atmosphere XII, 67450K, 2007.

Plant, W. J.: A stochastic, multiscale model of microwave backscatter from the ocean, Journal of Geophysical Research: Oceans, 107, 3120, https://doi.org/10.1029/2001JC000909, http://onlinelibrary.wiley.com/doi/10.1029/2001JC000909/abstract, 2002.

Protat, A., Pelon, J., Grand, N., Delville, P., Laborie, P., Vinson, J.-P., Bouniol, D., Bruneau, D., Chepfer, H., Delanoë, J., Haeffelin, M., Noel, V., and Tinel, C.: The Rali project: combining a radar and a lidar for the study of weakly-precipitating clouds, http://hdl.handle.net/2042/36076, 2004.

Protat, A., Bouniol, D., Delanoë, J., O'Connor, E., May, P. T., Plana-Fattori, A., Hasson, A., Görsdorf, U., and Heymsfield, A. J.: Assessment of Cloudsat Reflectivity Measurements and Ice Cloud Properties Using Ground-Based and Airborne Cloud Radar Observations, Journal of Atmospheric and Oceanic Technology, 26, 1717–1741, https://doi.org/10.1175/2009JTECHA1246.1, http://journals.ametsoc.org/doi/abs/10.1175/2009JTECHA1246.1, 2009.

Protat, A., Bouniol, D., O'Connor, E. J., Klein Baltink, H., Verlinde, J., and Widener, K.: CloudSat as a Global Radar Calibrator, Journal of Atmospheric and Oceanic Technology, 28, 445–452, https://doi.org/10.1175/2010JTECHA1443.1, http://journals.ametsoc.org/doi/abs/10.1175/2010JTECHA1443.1, 2010.

Protat, A., Delanoë, J., Strapp, J. W., Fontaine, E., Leroy, D., Schwarzenboeck, A., Lilie, L., Davison, C., Dezitter, F., Grandin, A., and Weber, M.: The Measured Relationship between Ice Water Content and Cloud Radar Reflectivity in Tropical Convective Clouds, Journal of Applied Meteorology and Climatology, 55, 1707–1729, https://doi.org/10.1175/JAMC-D-15-0248.1, http://journals.ametsoc.org/doi/abs/10.1175/JAMC-D-15-0248.1, 2016.

Ray, P. S.: Broadband complex refractive indices of ice and water, Applied Optics, 11, 1836, https://doi.org/10.1364/AO.11.001836, http://adsabs.harvard.edu/abs/1972ApOpt..11.1836R, 1972.

Riddle, A. C., Hartten, L. M., Carter, D. A., Johnston, P. E., and Williams, C. R.: A Minimum Threshold for Wind Profiler Signal-to-Noise Ratios, Journal of Atmospheric and Oceanic Technology, 29(7), 889–895, 2012.

Rosenkranz, P. W.: Water vapor microwave continuum absorption: A comparison of measurements and models, Radio Science, 33, 919–928, https://doi.org/10.1029/98RS01182, 1998.

Sadowy, G. A., Berkun, A. C., Chun, W., Im, E., and Durden, S. L.: Development of an advanced airborne precipitation radar, Microwave Journal, 46, 84–86, https://airbornescience.nasa.gov/sites/default/files/documents/pr2-mwj.pdf, 2003.

Stephens, G., Vane, D., Boain, R., Mace, G., Sassen, K., Wang, Z., Illingworth, A., O'Connor, E., Rossow, W., Durden, S., Miller, S., Austin, R., Benedetti, A., Mitrescu, C., and the CloudSat Science Team: The CloudSat mission and the A-train, Bull Amer Met Soc, 83, 1771–1790, 2002.

Stubenrauch, C. J., Rossow, W. B., Kinne, S., Ackerman, S., Cesana, G., Chepfer, H., Di Girolamo, L., Getzewich, B., Guignard, A., Heidinger, A., Maddux, B. C., Menzel, W. P., Minnis, P., Pearl, C., Platnick, S., Poulsen, C., Riedi, J., Sun-Mack, S., Walther, A., Winker, D., Zeng, S., and Zhao, G.: Assessment of Global Cloud Datasets from Satellites: Project and Database Initiated by the GEWEX Radiation Panel, Bulletin of the American Meteorological Society, 94, 1031–1049, https://doi.org/10.1175/BAMS-D-12-00117.1, http://journals.ametsoc.org/doi/abs/10.1175/BAMS-D-12-00117.1, 2013.

Tanelli, S., Durden, S. L., and Im, E.: Simultaneous Measurements of Ku- and Ka-Band Sea Surface Cross Sections by an Airborne Radar, IEEE Geoscience and Remote Sensing Letters, 3, 359–363, https://doi.org/10.1109/LGRS.2006.872929, http://adsabs.harvard.edu/abs/2006IGRSL...3..359T, 2006.

Tanelli, S., Durden, S. L., Im, E., Pak, K. S., Reinke, D. G., Partain, P., Haynes, J. M., and Marchand, R. T.: CloudSat's Cloud Profiling Radar After Two Years in Orbit: Performance, Calibration, and Processing, IEEE Trans-

actions on Geoscience and Remote Sensing, 46, 3560–3573, https://doi.org/10.1109/TGRS.2008.2002030, 2008.

Tyynelä, J., Leinonen, J., Moisseev, D., and Nousiainen, T. (2011). Radar Backscattering from Snowflakes: Comparison of Fractal, Aggregate, and Soft Spheroid Models, Journal of Atmospheric and Oceanic Technology, 28(11), 1365–1372, 2011.

Valenzuela, G. R.: Theories for the interaction of electromagnetic and oceanic waves — A review, Boundary-Layer Meteorology, 13, 61–85, https://doi.org/10.1007/BF00913863, https://link.springer.com/article/10.1007/BF00913863, 1978.

Vavriv, D. M., Volkov, V. A., Bormotov, V. N., Vynogradov, V. V., Kozhyn, R. V., Trush, B. V., Belikov, A. A., and Semenyuta, V. Y.: Millimeter-wave radars for environmental studies, Telecommunications and Radio Engineering, 61, http://www.dl.begellhouse.com/journals/0632a9d54950b268, 51ed66f435ca9ff2,1890baa935ca8045.html, 2004.

Vega, M. A., Chandrasekar, V., Nguyen, C., Mishra, K. V., and Carswell, J.: Calibration of the NASA Dual-Frequency, Dual-Polarized, Doppler Radar, 2012 IEEE International Geoscience and Remote Sensing Symposium, Munich, 4625–4628, https://doi.org/10.1109/IGARSS.2012.6350435, 2012.

Wu, J.: Mean square slopes of the wind-disturbed water surface, their magnitude, directionality, and composition, Radio Science, 25, 37–48, https://doi.org/10.1029/RS025i001p00037, http://onlinelibrary.wiley.com/doi/10.1029/RS025i001p00037/abstract, 1990.

Zhao, C., Xie, S., Klein, S. A., Protat, A., Shupe, M. D., McFarlane, S. A., Comstock, J. M., Delanoë, J., Deng, M., Dunn, M., Hogan, R. J., Huang, D., Jensen, M. P., Mace, G. G., McCoy, R., O'Connor, E. J., Turner, D. D., and Wang, Z.: Toward understanding of differences in current cloud retrievals of ARM ground-based measurements, Journal of Geophysical Research: Atmospheres, 117, D10 206, https://doi.org/10.1029/2011JD016792, http://onlinelibrary.wiley.com/doi/10.1029/2011JD016792/abstract, 2012.